This is the peer-reviewed, final accepted version for American Mineralogist, published by the Mineralogical Society of America.
The published version is subject to change. Cite as Authors (Year) Title. American Mineralogist, in press.
DOI: https://doi.org/10.2138/am-2022-8418. http://www.minsocam.org/

Revision 1

Gadolinium-dominant monazite and xenotime: selective hydrothermal enrichment of middle REE during low-temperature alteration of uraninite, brannerite and fluorapatite (the Zimná Voda REE-U-Au quartz vein, Western Carpathians, Slovakia)

Martin Ondrejka[1], Pavel Uher[1], Štefan Ferenc[2], Stanislava Milovská[3], Tomáš Mikuš[3], Alexandra Molnárová[1], Radek Škoda[4], Richard Kopáčik[2], Peter Bačík[1]

[1]*Department of Mineralogy Petrology and Economic Geology, Faculty of Natural Sciences, Comenius University, Ilkovičova 6, Mlynská dolina, 84215, Bratislava, Slovakia*

[2]*Department of Geography and Geology, Faculty of Natural Sciences, Matej Bel University, Tajovského 40, 97401 Banská Bystrica, Slovakia*

[3]*Earth Science Institute, Slovak Academy of Sciences, Ďumbierska 1, 97401, Banská Bystrica, Slovakia*

[4]*Department of Geological Sciences, Faculty of Science, Masaryk University, Kotlářská 2, 61137 Brno, Czech Republic*

ABSTRACT

A hydrothermal quartz vein with REE-U-Au mineralization in the Zimná Voda (Gemeric Unit, Western Carpathians, Slovakia) is associated with contact metamorphism between Permian granites and host phyllites and metaquartzites. It contains unique REE minerals from the monazite and xenotime groups. Monazite-(Ce), monazite-(Nd), monazite-(Sm), and Gd-dominant monazite ["monazite-(Gd)"], along with xenotime-(Y) to Gd-dominant xenotime ["xenotime-(Gd)"] and Gd-rich hingganite-(Y) show heterogeneous compositions and reflect a strong fractionation trend toward the enrichment of MREE (Sm to Dy), particularly Gd. Here, the gadolinium abundance reported in "monazite-(Gd)" (≤23.4 wt% Gd_2O_3) and Gd-rich xenotime-

(Y) to "xenotime-(Gd)" (≤28.7 wt% Gd_2O_3) and accompanied by Gd-rich hingganite-(Y) (≤15.8 wt% Gd_2O_3), is among the highest Gd concentrations ever reported in natural minerals. The Gd-richest compositions show the following formulae:

$(Gd_{0.31}Sm_{0.24}Nd_{0.15}Ce_{0.10}La_{0.05}Dy_{0.03}Y_{0.03}\ldots)_{0.98}PO_4$ ["monazite-(Gd)"],

$(Gd_{0.36}Y_{0.32}Dy_{0.13}Sm_{0.08}Tb_{0.05}\ldots)_{0.98}(P_{0.96}As_{0.04})_{1.00}O_4$ ["xenotime-(Gd)"] and

$(Y_{0.71}Gd_{0.43}Dy_{0.23}Sm_{0.22}Tb_{0.06}Er_{0.04}Nd_{0.06}\ldots Ca_{0.06})_{1.96}(_{0.87}Fe^{2+}_{0.13})_{1.00}(Be_{1.82}B_{0.18})_{2.00}(Si_{1.90}As_{0.10})_{2.00}O_8(OH_{1.70}O_{0.30})_{2.00}$ [hingganite-(Y)]. The MREE-rich monazites, xenotimes, and hingganite-(Y) precipitated in response to the alteration of primary uraninite, brannerite, and fluorapatite by low-temperature hydrothermal fluids of heterogeneous compositions on a micro-scale. These are responsible for the strong enrichment of individual MREE, especially Gd in the secondary minerals. This is accompanied by the advancing development of the W-type tetrad effect on REE through monazite species. The substantial incorporation of Gd into both REE-selective monazite and xenotime structures that are accompanied by LREE vs. HREE segregation indicates the possibility of differently-sized REE^{3+} miscibility in $REEPO_4$ solid solutions, as well as the stabilization of the Gd-rich orthophosphate structure by substitution of the remaining *A*-site cations with smaller HREE+Y in the xenotime-type, and/ or larger LREE in the monazite-type structure.

Keywords: monazite, xenotime, hingganite, Gd-enrichment, REE fractionation, MREE enrichment, tetrad effect, Western Carpathians

INTRODUCTION

Accessory monazite-group minerals (MGM) and xenotime-group minerals (XGM) are widespread in numerous lithologies, including various magmatic, metamorphic, and sedimentary rocks, as well as hydrothermal, authigene, and supergene systems. Monazite contains dominant trivalent LREE (light Ln: La–Sm) based on their preference of monazite-type crystal structure (Ni et al. 1995). Among them, monazite-(Ce) is the most common end-member, whereas monazite-(La), monazite-(Nd), and monazite-(Sm) occur as rare minerals only in specific pegmatite, post-magmatic or sedimentary environments (e.g., Graeser and Schwander 1987; Demartin et al. 1991b; Pekov 2000; Massau et al. 2002; Dowman et al. 2017). There are only two known end-members in the XGM. Xenotime-(Y) is by far the most widespread and contains the dominant Y^{3+}, as well as usually low contents of other HREE (heavy Ln, Tb–Lu) and negligible amounts of LREE. On the other hand, xenotime-(Yb) and Yb-, Dy-, and Gd-rich xenotime-(Y) belong to very rare minerals occurring in some granitic pegmatites and metamorphic-hydrothermal lithologies (Demartin et al. 1991a; Förster and Rhede 1995; Förster 1998b; Buck et al. 1999; Massau et al. 2000; Repina 2011, 2014; Franz et al. 2015). Despite having a generally coherent behavior, selective REE mobilization and fractionation in aqueous systems is quite common and has been reported previously from different geochemical environments (e.g., Seredin 1996; Morgan et al. 2012; Lee et al. 2013; Franz et al. 2015; Migdisov et al. 2019; Ondrejka et al. 2018; Abedini et al. 2019; Anenburg et al. 2020b).

Here, we describe a unique case of substantial middle REE (MREE, Sm–Dy) enrichment and localized Gd-predominance in monazite, xenotime, and Gd-rich hingganite-(Y), which is due to the low-temperature alteration of primary uraninite, brannerite and fluorapatite, as well as the subsequent remobilization and precipitation of REE by aqueous media from the hydrothermal REE-U-Au quartz vein in Zimná Voda near Prakovce, eastern Slovakia. This study presents the

first description of exceptionally Gd-rich monazite to Gd-dominant "monazite-(Gd)", as well as Gd-, Dy-rich xenotime-(Y) to "xenotime-(Gd)" and Gd-rich hingganite-(Y) based on detailed EPMA study; all phases belong to the highest published Gd contents in natural minerals. Moreover, "monazite-(Gd)" and "xenotime-(Gd)" are potential new minerals. A detailed structural study, which is necessary for its approval by the IMA-CNMNC, will be the subject of our future investigation. To date, lepersonnite-(Gd), which is a rare REE-uranyl carbonate from the Shinkolobwe U deposit in the DR Congo (Deliens and Piret 1982), represents the only approved Gd-dominant mineral found in nature.

REGIONAL GEOLOGY

The investigated Zimná Voda occurrence is located in the Lower Paleozoic metamorphic rocks of the Bystrý Potok Formation, a part of the Gelnica Group in the Gemeric tectonic Unit of the Western Carpathians, which is part of the Alpine-Carpathian Mountain belt (Fig. 1a). The Gelnica Group is represented by a several-thousand metre thick Paleozoic flysch sequence with important rhyolite-dacite admixture (Ivanička et al. 1989). These rocks have undergone regional metamorphism under lower greenschist-facies conditions (Faryad 1991). The Bystrý Potok Fm. (Ordovician to Silurian) is formed mainly by black cherts, quartz-sericite or graphitic phyllites, greywackes, metarhyolites and tuffites, rarely by actinolite shales (Bajaník et al. 1983; Ivanička et al. 1989), Fig. 1b. The metavolcanic rocks yielded Middle Ordovician U–Pb SHRIMP zircon ages (~460–465 Ma; Vozárová et al. 2010). These metamorphic rocks are intruded by Permian Gemeric granites (~260–270 Ma; e.g., Villaseñor et al. 2021).

The Zimná Voda REE-U-Au vein mineralization is located near the main ridge of the Slovenské Rudohorie Mts. approximately 5.6 km to the S of the village of Prakovce and 600 m to

the NW of the elevation point Tri Studne and an altitude of ~950 m. The geographical coordinates of the occurrence are 48.767°N and 20.913°E.

Two quartz veins (Western and Eastern) containing U and Au mineralization were found in the area. The subject of our research focused on the more significant Western vein. The vein is located in sericitic phyllites, with interbeds of fine-grained metaquartzites. These metamorphic rocks are intruded by Permian granites in the Hummel site, ~600 m to the SW of the Zimná Voda occurrence. The Western vein conforms to the metamorphic schistosity of the surrounding rocks. It has an E–W direction, as well as a total length of ~90 m with an average inclination of 65° to the S. The thickness of the vein ranges from 3 to 30 cm. The vein is slightly corrugated and segmented by transverse faults into segments of 3 to 55 m long, while termination of the vein on both tails is also tectonic. Drilling surveys showed a tectonic zone cutting the vein at a depth of 7–10 m. The main vein body is accompanied by short veinlets with U-Au mineralization, and quartz veins without ore mineralization. The host rocks are hydrothermally-altered with disseminated pyrite in a contact zone that is 2 to 8 m wide. Along the contact, the rocks are intensively sericitized and locally silicified. Both the quartz veins with ore mineralization and the host rocks are intensively limonitized.

In addition to dominant quartz, the following minerals were identified in the veins (Rojkovič et al. 1997): uraninite, brannerite, rutile, gold, bismuth, bismuthinite, pyrite, arsenopyrite, cobaltite, glaucodot, molybdenite, galena, tetrahedrite-(Fe), fluorapatite, monazite-(Ce), xenotime-(Y), muscovite, chlorite, and tourmaline; supergene minerals are represented by goethite, trögerite(?), zeunerite, and scorodite. The maximum U content detected in the ore was 11850 ppm (3076 ppm in average), the Au content ranges ≤3500 ppm, 38 ppm on average (Rojkovič et al. 1997). The mineralization probably originated by fluid-driven hydrothermal

mobilization of REE, U, and Au from the surrounding metamorphic rocks by intrusion of the Permian granitic rocks (Rojkovič et al. 1997, 1999).

METHODS

The field samples were collected from old exploration trenches using an SGR scintillation radiometer. Hand-specimen sized pieces were sampled and numbered from ZV-1 to ZV-6. The mineral assemblages and textures were identified by electron probe microanalysis (EPMA) and observed using back-scattered electron (BSE) image. The Gd-predominance in minerals was identified only in one sample (ZV-2). In total, 10 polished thin sections of this sample were studied in detail.

Chemical composition of the minerals was studied by EPMA in wavelength-dispersive spectrometry (WDS) mode, and X-ray elemental mapping using a JEOL JXA-8530F electron microprobe at the Earth Science Institute, Slovak Academy of Sciences in Banská Bystrica, Slovakia. An accelerating voltage of 15 kV and a probe current of 20 nA were used. The typical spot beam diameter varied from 2 to 8 μm; a more focused ≤1–3 μm beam was used only occasionally to avoid any intermediate composition in strongly heterogeneous micro-scale areas. A series of X-ray elemental maps was acquired with different resolution (0.06–0.23 μm/pixel) and dwell time (30–100 ms). The EPMA was calibrated using natural and synthetic standards (Supplementary Table 1), and raw counts were converted to wt% of oxides using *ZAF* matrix correction. The WDS scan of peak and background positions for selected REE elements analyzed are shown in Supplementary Figure 1. Corrections of line interferences were provided using the method by Åmli and Griffin (1975). The detection limit for all elements is typically between 0.01 and 0.02 wt%.

Element contents in the mineral formulae are expressed in atoms per formula unit (apfu). The uraninite formula was normalized to 2 oxygen atoms, brannerite to 3 cations, and the partition of total uranium between U^{4+} and U^{6+} in brannerite was calculated from a neutral charge balance. Fluorapatite was calculated based on Σ(M+T) = 8 cations and OH+F+Cl = 1 apfu (Pasero et al. 2010). The monazite and xenotime formulae were normalized to 4 oxygen atoms. The gadolinite-supergroup nomenclature (Bačík et al. 2017) is used for hingganite-(Y) formula calculation, normalized on the basis of A = 2 cations (general chemical formula: $A_2MQ_2T_2O_8\varphi_2$). The B_2O_3 and BeO contents (wt%) were calculated from the charge balance according to Be = 6 – [20 – ΣPC – OH] (where PC is the sum of charges for all cations except B and Be) and B = 2 – Be. REE patterns were fitted, and tetrad effect were calculated using BlambdaR/ AlambdaR method (Anenburg 2020; Anenburg and Williams 2022).

RESULTS

Uraninite

Primary hypogene uraninite (uraninite I) UO_2 is an abundant mineral and, together with brannerite, the most important U carrier. It usually forms large botryoidal aggregates (≤1.2 mm in size) and microcrystalline masses with globular microstructures, often showing concentric bands (pitchblende variety) with numerous desiccation cracks filled with quartz, brannerite, or supergene uranyl arsenates-phosphates formed due to the oxidation-hydration alteration of uraninite (Figs. 2a–2d and 3a). The relatively homogeneous chemical composition close to the theoretical UO_2 end-member is a characteristic feature of uraninite I. While the U content varies between 83.0 and 90.6 wt% UO_2 (0.65–0.92 apfu U), the Th concentrations are negligible (≤0.1 wt% ThO_2) (Table 1 and Supplementary Table 2). The Y content is relatively low (≤1.0 wt% Y_2O_3, 0.03 apfu Y) and other REE attain 2.9 wt% REE_2O_3 (0.04 apfu REE). The distribution of

REE within the botryoidal aggregate suggests their partial removal in altered central parts and rims (Figs. 3b and 3c). The average chondrite-normalized REE pattern of uraninite I shows relative enrichment in MREE and corresponding depletion in LREE and HREE (Fig. 4a). Uraninite I is W-rich (1.6–4.2 wt% WO_3, ≤0.04 apfu W), low concentrations of Mo, As and Fe are usually detected (Table 1 and Supplementary Table 2). In situ U–Th–total Pb EPMA age determination of uraninite I gave a Triassic (Anisian) age of 246±0.6 Ma (n=42, MSWD: 8.0; Ondrejka et al. in prep.).

Secondary uraninite II forms alteration rims around uraninite I (Figs. 2a, 2b and 2d), or partly recrystallized, metamict(?) and hydrated domains in the central parts of uraninite I (Figs. 2c and 2d). It shows more complex internal microtexture characterized by porosity and fractures. Uraninite II has a strongly heterogeneous composition, low totals and non-ideal stoichiometry with ≤9.3 wt% WO_3, ≤3.2 wt% Sb_2O_5, ≤3.7 wt% FeO, ≤7.0 wt% Y,REE_2O_3, ≤2.7 wt% As_2O_5, but low P and Si contents.

The youngest uraninite III is represented by newly-formed tiny crystals (0.5–8 μm in size), which form clusters in the proximity of uraninite I (Figs. 2a, 2d and 2g), or disseminated inclusions within the REE phosphates (Figs. 5a and 5c). It is characterized by an elevated Y content (2.5–5.8 wt% Y_2O_3, ≤0.14 apfu Y) and other REE (1.9–6.6 wt% REE_2O_3, ≤0.1 apfu REE); while the concentration of other trace elements (Si, W, Mo, Sb) are negligible and mostly below the detection limit (Table 1 and Supplementary Table 2).

Brannerite

Brannerite, ideally UTi_2O_6, is a common mineral at Zimná Voda and the main U carrier together with uraninite. It usually forms the fillings of cavities, desiccation cracks, and the central

parts of the uraninite aggregates (Fig. 2a) or large and disseminated crystals, as well as cataclased quartz-brannerite aggregates (≤1 mm in size) in close association with gold and uraninite (Figs. 2e and 2f). The chemical composition of primary brannerite I is relatively uniform and varies within 0.2–1.7 wt% REE_2O_3 (≤0.05 apfu REE). Tungsten (≤3.4 wt% WO_3, ≤0.07 apfu W) and Sb (≤1.2 wt% Sb_2O_5, ≤0.03 apfu Sb) are always present; locally slightly elevated Nb content was detected (≤2.0 wt% Nb_2O_5, ≤0.07 apfu Nb).

Some crystals of brannerite consist of two generations, where unaltered brannerite I forms the outer zone of the crystals, while altered domains of brannerite II are located in their central parts (Fig. 2f). Brannerite II differs from brannerite I mainly in U and REE concentrations; brannerite II shows lower U (22.7–39.8 wt% UO_2, 0.36–0.62 apfu U), but markedly higher REE (4.4–8.4 wt% REE_2O_3, 0.12–0.26 apfu REE), especially Y and Gd (≤4.2 wt% Y_2O_3, 0.16 apfu Y and 2.5 wt% Gd_2O_3, 0.06 apfu Gd), as well as higher Sb, Nb, Si, Al, Fe, and Mn contents (Table 1 and Supplementary Table 3). The chondrite-normalized REE pattern shows typical MREE enrichment in a secondary (altered) assemblage (Fig. 4b). The brannerite II analyses reveal low oxide totals (~80–93 wt%) in comparison to brannerite I (94–98 wt%), which likely indicates its hydrated and metamict nature (Table 1 and Supplementary Table 3).

Fluorapatite

Primary fluorapatite is an abundant hypogene phosphate mineral and occurs as subhedral or anhedral crystals (≤100 μm in size) that are closely associated with other REE phosphates and Fe arsenates scattered in the quartz-muscovite matrix (Fig. 2g). The chemical composition of fluorapatite is relatively uniform: ≤0.6 wt% REE_2O_3 (≤0.02 apfu REE) and ≤0.2 wt% Y_2O_3 (≤0.01 apfu Y) reflecting only negligible input of the britholite and/or belovite components. The

208 average of the chondrite-normalized REE pattern shows relative enrichment in MREE and
209 corresponding depletion in LREE and HREE (Fig. 4c). The F/(F+OH) atomic ratio attains 0.93 to
210 1.00 and ≤0.1 wt%. The compositions show very low amounts of other divalent cations (Mn, Sr,
211 Mn; Table 1 and Supplementary Table 4).
212
213 **Monazite-group minerals**
214 The MGM are the main LREE carriers in the Zimná Voda occurrence. They form numerous
215 crystals or crystal aggregates (≤150 μm in size), usually as intergrowths with xenotime-(Y),
216 fluorapatite, and uraninite III (Figs. 5a–5d and 5f). Four members of MGM could be recognized:
217 monazite-(Ce), the most common and the only LREE phosphate in all the samples except for ZV-
218 2, whereas, monazite-(Nd), monazite-(Sm), and "monazite-(Gd)" occur only in the ZV-2 sample
219 (Fig. 5d). The monazite-type structure of these species has been confirmed by micro-Raman
220 spectroscopy (see Supplementary Material). The composition of individual crystals is relatively
221 homogeneous without any distinct variations in the core-rim profile. However, a heterogeneous
222 composition reflecting irregular zones of different REE distribution may occur locally (Fig. 3d-
223 3i).
224 The MGM have the following major REE proportions: monazite-(Ce) has compositions with
225 Ce>Nd>Sm>Gd (16–26 wt% Ce_2O_3, 0.23–0.37 apfu Ce; 3–10 wt% Gd_2O_3, 0.03–0.13 apfu Gd).
226 Monazite-(Nd) shows compositions with Nd>Sm~Ce>Gd (15–25 wt% Nd_2O_3, 0.21–0.35 apfu
227 Nd; 5–13 wt% Gd_2O_3, 0.06–0.16 apfu Gd). Monazite-(Sm) reveals Sm>Gd~Nd>Ce (15–20 wt%
228 Sm_2O_3, 0.20–0.27 apfu Sm; 10–19 wt% Gd_2O_3, 0.13–0.25 apfu Gd). Finally "monazite-(Gd)"
229 displays Gd>Sm>Nd>Ce (17–23 wt% Gd_2O_3, 0.22–0.31 apfu Gd; 15–19 wt% Sm_2O_3, 0.20–0.25
230 apfu Sm) (Table 1 and Supplementary Table 5). In general, the element distribution in MGM

231 shows an enrichment trend from La–Nd to Sm–Dy with Sm~Gd>Nd>Ce>La (MREE>LREE)
232 and equally negligible Ho–Lu (HREE)+Y abundances (Fig. 6). Although different REE^{3+} are the
233 dominant cations in the corresponding MGM members, their chondrite-normalized REE patterns
234 exhibit the conspicuous maxima at Sm and Gd. However, the patterns of Nd-, Sm-, and Gd-
235 dominant monazite are partly distinct from monazite-(Ce), which shows a less clear maximum at
236 Sm, but more enriched in La and Ce and conspicuously depleted in HREE (Fig. 4d).
237 Interestingly, there are also distinct differences in the shape of the first tetrad (La-Ce-Pr-Nd)
238 which shows a downward concave W-type curvature, progressively developing from monazite-
239 (Ce) to "monazite-(Gd)" with average t1 = 0.63, (Mnz-Ce) to t1 = 8.64 ("Mnz-Gd") in the ZV-2
240 sample (calculation sensu Minami and Masuda 1997; Fig. 4e).
241 Yttrium is generally low (≤1.0 wt% Y_2O_3; ≤0.02 apfu Y, occasionally ≤4.0 wt% Y_2O_3; ≤0.08
242 apfu Y) and actinides are very low, (≤0.3 wt% ThO_2+UO_2; occasionally ≤3.2 wt%; ≤0.03 apfu
243 Th+U). Some crystals contain slightly elevated As (≤1.3 wt% As_2O_5; ≤0.03 apfu As) and Fe
244 (≤2.2 wt% FeO_{total}; ≤0.07 apfu Fe). Other trace elements (Ca, Si, S, and Sr) have negligible
245 concentrations, or they are below detection limits (Table 1 and Supplementary Table 5).
246
247 **Xenotime-group minerals**
248 In the studied occurrence, the XGM are the main Y+HREE carrier together with rare
249 hingganite-(Y). They form numerous crystals and massive aggregates (≤100 μm in size), usually
250 as intergrowths with MGM and with tiny inclusions of uraninite, or in close association with
251 uranyl arsenates or phosphates (Figs. 5a–5g). Xenotime-(Y) usually forms central parts of
252 crystals (xenotime I), whereas Gd-rich xenotime-(Y) to Gd-dominant "xenotime-(Gd)" (xenotime
253 II) are located in the marginal parts of the aggregates or as veinlets in xenotime I (Figs. 3j-3o and

This is the peer-reviewed, final accepted version for American Mineralogist, published by the Mineralogical Society of America.
The published version is subject to change. Cite as Authors (Year) Title. American Mineralogist, in press.
DOI: https://doi.org/10.2138/am-2022-8418. http://www.minsocam.org/

Figs. 5a–5d, 5f, 5g). The xenotime-type structure of these species has been confirmed by micro-Raman spectroscopy (see Supplementary Material).

In contrast to MGM, the XGM display mostly irregular and convolute zonation in some places, as well as heterogeneous composition reflecting different Y/(Gd+Dy) and locally (U+Th)/REE growth zone ratios. This observed core-rim chemical heterogeneity of individual XGM crystals contrasts markedly with MGM. The distribution of Y, Gd, and Dy generally clusters XGM into the following groups: xenotime I is characterized by high Y content (35–46 wt% Y_2O_3, 0.64–0.81 apfu Y) and relatively low content of Gd and Dy (≤8.5 wt% Gd_2O_3, ≤0.1 apfu Gd and ≤8.4 wt% Dy_2O_3, ≤0.09 apfu Dy, respectively); whereas xenotime II contains low Y (18–33 wt% Y_2O_3, 0.37–0.61 apfu Y) and elevated Gd, Dy and Tb (11.5–28.7 wt% Gd_2O_3, 0.13–0.36 apfu Gd; 7.9–14.4 wt% Dy_2O_3, 0.09–0.17 apfu Dy and 4.0 wt% Tb_2O_3, 0.05 apfu Tb) (Table 1 and Supplementary Table 6; Fig. 6). The compositions with slight atomic dominance of Gd over Y (0.34–0.36 apfu Gd vs. 0.31–0.34 apfu Y), which corresponds to "xenotime-(Gd)" were detected in four analyses (Fig. 7).

The chondrite-normalized REE pattern of xenotime I shows a different REE distribution compared to xenotime II (Fig. 4f). It has the most extensive M-type tetrad effect on t3 and t4 tetrads with average t3 = -4.74 and t4 = -8.44 (Fig. 4g). The Gd-rich xenotime II has a significant upward convex MREE pattern with a maximum in Gd and a less distinct M-type tetrad effect signature compared to xenotime I (Fig. 4f). Uranium has an average value 0.5 wt% UO_2 in xenotime I and 0.7 wt% UO_2 in xenotime II. Thorium concentration in xenotime I+II is below the detection limits. Some crystals of xenotime II contain slightly elevated As (≤2.3 wt% As_2O_5) and Fe (≤2.5 wt% FeO_{total}) (Table 1 and Supplementary Table 6).

This is the peer-reviewed, final accepted version for American Mineralogist, published by the Mineralogical Society of America.
The published version is subject to change. Cite as Authors (Year) Title. American Mineralogist, in press.
DOI: https://doi.org/10.2138/am-2022-8418. http://www.minsocam.org/

Hingganite-(Y)

Hingganite-(Y), ideally [$Y_2\square Be_2Si_2O_8(OH)_2$] is a rare mineral and sporadically present in the quartz-muscovite gangue. It usually forms large solitary crystals (≤300 μm in size). It has mostly irregular zonation and strongly heterogeneous composition in BSE, reflecting different Y/(Gd+Sm) growth zone ratio (Figs. 3p, 3r and Fig. 5h). The dark domains (hingganite I) are strongly Y-dominant in composition (26.2–30.9 wt% Y_2O_3, 1.2–1.4 apfu Y). Other major REE cations at A-site are Dy (8.8–10.4 wt% Dy_2O_3; ≤0.3 apfu Dy) and Gd (3.7–7.4 wt% Gd_2O_3, ≤0.2 apfu Gd). The bright domains (hingganite II; Fig. 5h) are richer in MREE, particularly in Gd (≤15.8 wt% Gd_2O_3, ≤0.4 apfu Gd) and Sm (≤9.7 wt% Sm_2O_3, ≤0.3 apfu Sm; Table 1 and Supplementary Table 7, Fig. 6). The chondrite-normalized REE patterns of both hingganites show a very similar convex shape with the hump on MREE and with the maximum in Gd and Tb respectively (Fig. 3h). Additionally, Y+REE, Ca is the other cation present at the A-site in low amounts (0.5–0.8 wt% CaO, ≤0.08 apfu Ca) (Fig. 8). Hingganite I+II shows a characteristic dominant M-site vacancy (0.51–0.63 pfu); however, two analyses show dominant Fe^{2+} at M-site (vac. 0.48–0.49 pfu) and correspond to gadolinite-(Y). In general, the M-site is partly occupied by Fe (5.8–7.7 wt% FeO, ≤0.52 apfu Fe), since all other possible cations are below 0.01 apfu (Table 1 and Supplementary Table 7).

DISCUSSION

Gd and MREE abundances in natural minerals

Gadolinium-dominant and Gd-rich minerals are generally quite rare in nature due to the low, absolute abundance of Gd, which is relative to other, more abundant REE (especially Ce, Nd, La, Y) in the Earth's upper crust (e.g., Hazen et al. 2015). This includes the relatively strong,

coherent lanthanides partitioning, which is dependent mainly on charge and ionic radius-controlled behavior (CHARAC) (Bau 1996; Rezaei Azizi et al. 2017). Selective enrichment of Gd or other individual MREE and HREE in terms of absolute abundances is a rare process and does not appear to be related to specific lithologies and environments (cf. Demartin et al. 1993; Massau et al. 2000; Čopjaková et al. 2011; Hannigan and Sholkowitz 2001; Grawunder et al. 2014; Franz et al. 2015).

The only IMA-CNMNC approved, naturally-occurring Gd-dominant mineral is lepersonnite-(Gd), $CaGd_2(UO_2)_{24}(CO_3)_8Si_4O_{28}\cdot 60H_2O$ (Deliens and Piret 1982), which, however, contains a relatively low absolute concentration of essential Gd (2.1 wt% Gd_2O_3) together with minor Dy, Y, and Tb. On the other hand, the extent of enrichment of Gd (La, Nd, and Sm) in MGM and Gd (Yb and Dy) in XGM is usually ≥10 wt% REE_2O_3. The highest Gd_2O_3 content in MGM described to date is most likely 13.5 wt% (accompanied by 14.3 wt% Sm_2O_3) in monazite-(Sm) from its type locality of Annie Claim, Manitoba, Canada, where it occurs in a lepidolite-subtype granitic pegmatite (Massau et al. 2002). The highest Gd_2O_3 content in xenotime-(Y) noted to date is 25 wt% from the quartz vein of Au-REE mineralization in the Nether-Polar Urals, Russia (Repina 2010, 2011) and 12.6 wt% in gadolinite-(Y) from Alpine fissures in Glogstafelberg, Val Formazza, Italy (Demartin et al. 1993).

Our reported Gd abundances in MGM (≤23.4 wt% Gd_2O_3) and XGM (≤28.7 wt% Gd_2O_3), accompanied by Gd-rich hingganite-(Y) (≤15.8 wt% Gd_2O_3) from the Zimná Voda REE-U-Au quartz vein mineralization represent the highest Gd concentrations in these minerals worldwide, and are documented by appropriate methods and corresponding analytical data. We emphasize the use of appropriate and precise analytical methods, since there are published data that document the possible presence of other Gd-dominant minerals; unfortunately without suitable

analytical method or measurements. The presence of Gd-dominant monazite with 42.5 wt% Gd_2O_3 and empirical formula $(Gd_{0.55}Y_{0.25}Dy_{0.1}Sm_{0.05}Nd_{0.05}Th_0Ca_0)(PO_4)$ is noted from alkali-feldspar syenite pegmatite at the Myan Gyi mine, near Mogok, Myanmar (Kartashov, web data at mineralienatlas.de; mindat.org); however, without any further information. The impressive REE accumulations in lignite coals from the Russian Far East Pavlovka deposit contain fine-grained authigenic unknown Gd- and Dy-dominant minerals (Seredin 1992). Several nano- to micro-sized particles of Gd-Ti-Zr oxides with dominant Gd occupancy and 9–57 wt% Gd_2O_3 were identified in the lunar regolith from Mare Crisium (Bogatikov et al. 2004; Mokhov et al. 2011). In addition, an unnamed Gd-dominant mineral (Gd>Ce>La) close to the $Gd_2Ti_4O_{11}$ formula was noted from fumaroles in the active Kudriavy Volcano, Kuril Islands, Russia (Bogatikov et al. 2004). However, all the above-mentioned findings of possible Gd-dominant minerals need to be taken and interpreted with caution, because the data were obtained using semi-quantitative EDX analysis without appropriate analytical details. Furthermore, other analytical data (e.g., XRD, micro-Raman) are lacking.

Gd and MREE incorporation in monazite and xenotime

A large amount of literature exists on the crystal chemistry of natural and synthetic monazite- and xenotime-type structures with the general formula APO_4 (e.g., Mullica et al. 1990; Ni et al. 1995; Kolitsch and Holtstam 2004; Clavier et al. 2011; Muñoz and Rodríguez-Hernández 2018 and references therein). There is general consensus that the pure end-members containing larger, nine-fold coordinating LREE cations crystallize with the monoclinic monazite-type structure, whereas those members with smaller HREE+Y cations in eight-fold coordination have a tetragonal xenotime- (or zircon)-type structure, and the boundary between these two

346 orthophosphate structure types usually lies between Gd and Tb (e.g., Ni et al. 1995; Gratz and
347 Heinrich 1998; Hay et al. 2013; Rodriguez-Liviano et al. 2013). Thus, Tb is the largest REE
348 cation that the xenotime-type structure accommodates. However, the dimorphism of Gd- to Ho-
349 phosphates exists and depends on the conditions of formation, mainly the temperature of
350 precipitation, REE precursor, and pH of the solution (Kolitsch and Holtstam 2004; Boakye et al.
351 2008; Rodriguez-Liviano et al. 2013).

352 Monazite-group minerals from Zimná Voda, along with the significant Gd content, also
353 exhibit overall LREE>HREE signature, whereas xenotime is mostly Y-dominant and has
354 HREE>LREE signature. It suggests the substantial incorporation of Gd into both REE-selective
355 structures. These findings confirm the aforementioned earlier studies of differently-sized REE^{3+}
356 substitution in $REEPO_4$ solid solutions and the stabilization of the Gd-rich orthophosphate with
357 xenotime-type structure by substitution of the rest of the A-site cations for smaller HREE+Y and
358 vice versa (Mullica et al. 1986, 1990; Gratz and Heinrich 1998; Rodriguez-Liviano et al. 2013).
359 Conclusively, the stabilization of monazite- vs. xenotime-type structure of the natural $REEPO_4$
360 species depends on the average REE^{3+} ionic radius (Kolitsch and Holtstam 2004). In addition, the
361 xenotime-type structure of synthetic Gd-dominant phosphate doped by Tb, Y, Er, and Yb has
362 been documented by earlier studies (Mullica et al. 1986, 1990; Gratz and Heinrich 1998).
363 Moreover, the synthesis of pure $GdPO_4$ nanoparticles with tetragonal structure, has also been
364 previously reported (Rodriguez-Liviano et al. 2013). However, the possible impact on the
365 structural stability of commonly observed impurities, e.g., Th, U, Ca, Si, and S (cf. Demartin et
366 al. 1991a, 1991b; Förster 1998a, 1998b; Kolitsch and Holtstam 2004; Ondrejka et al. 2007;
367 Clavier et al. 2011) in the Zimná Voda MGM and XGM is probably not important, since the
368 concentrations of these elements are negligible (Supplementary Tables 5 and 6). Only As

concentration in some Gd-rich xenotimes are slightly higher than average (≤0.045 apfu As), which could result in similar stabilization effects toward the xenotime-type structure and suggests that the behavior of the $REEAsO_4$ compound is different from those of the $REEPO_4$ compounds (cf. Kolitsch and Holtstam 2004 and references therein).

Origin of Gd and MREE enrichment

The reported selective enrichment of Gd and other MREE in REE-U-Au vein mineralization at Zimná Voda is an extremely rare process which occurred as a rather, localized anomaly in the ZV-2 sample only, though in multiple thin sections. Other samples collected from the same site, contain either a non- or less-fractionated composition of monazite-(Ce) and xenotime-(Y) with respect to the ZV-2 sample. The dramatic increase of the local Gd concentration is linked to the gradual decrease of the most common Ce (redox sensitive element) along with La, Pr, and Nd in MGM. This cannot be fully explained solely by selective fractionation of REE due to the oxidation of Ce^{3+} to Ce^{4+} and removal of CeO_2 from the solution (Fisher and Meyrowitz 1962; Banfield and Eggleton 1989; Braun et al. 1990; Mayer et al. 2014; MacDonald et al. 2015; Ondrejka et al. 2018), since the Ce negative anomaly did not develop in the chondrite-normalized REE patterns of the studied minerals (Fig. 4). However, a coherent depletion on the first tetrad in MGM developed instead. This indicates the possible appearance of a concave W-type tetrad effect that occurs rarely, and together with the low Th content, supports the hypothesis of hydrothermal crystallization from a low-temperature aqueous solution (e.g., Takahashi et al. 2002; Schandl and Gorton 2004; Zhao et al. 2010).

The compositional heterogeneity and variable enrichment in Gd and other individual REE, particularly Sm in MGM, Dy, and Tb in xenotime-(Y), as well as Sm in hingganite-(Y) display

392 the expressive positive anomalies of Sm and Gd (less distinctive Dy and Tb) that are relative to
393 adjacent normalized values. This hump in MREE (a convex shape or "MREE bulge") is a
394 characteristic and remarkable feature of all late-crystallized REE minerals herein and most likely
395 results from a localized, yet strong progressive decoupling of LREE+HREE and MREE on
396 relatively small scales (cf. Anenburg 2020). The heterogeneous fluid composition on a micro
397 scale, as well as the development of variations in the local chemical environment responsible for
398 the strong enrichment of individual REE is most likely (cf. Franz et al. 2015). The textural-
399 compositional characteristics, which are generally dominant Ce and Y contents in the central
400 parts of the monazite and xenotime crystals, but lower in the outer parts and in younger veinlets
401 that cut the early-crystallized REE minerals, including the progressive fractionation trend toward
402 MREE in late-crystallized grains/domains, indicate the early crystallization of monazite-(Ce)
403 together with xenotime-(Y) I until Gd-predominance and MREE enrichment was achieved.
404 The reason for such extremely unusual MREE enrichment is not obvious; however, the
405 alteration of hypogene MREE-selective minerals (uraninite I, brannerite I ± fluorapatite, and
406 hingganite I) by late hydrothermal fluids or groundwater solutions can be responsible for such
407 REE remobilization and low-temperature MREE enrichment. The REE were probably mobilized
408 from these primary minerals, which are significant host phases for REE, especially when taking
409 into consideration their low REE content, yet high modal abundances. Here, uraninite, brannerite,
410 and fluorapatite show MREE-enriched chondrite-normalized patterns (Figs. 4a–4c). Such MREE-
411 enriched pattern is typical for hydrothermal apatite and differs from magmatic LREE-rich apatite
412 with a strong Eu anomaly (e.g., Krneta et al. 2017; Anenburg et al. 2020a). Primary hingganite I
413 also contributed to bulk MREE enrichment, even though it is rare in abundance and has a high
414 total REE content and distinct MREE-enriched pattern (Fig. 4h). During uraninite I precipitation,

415 the value of ionic radius of U^{4+} under reducing conditions in eight-fold coordination (1.00 Å) is
416 similar to those of trivalent Gd (1.05 Å) and Tb (1.04 Å) (Shannon 1976). Therefore, in
417 comparison with other REE, Gd^{3+} may have similar crystal-chemical properties as U^{4+} (cf.
418 Hidaka et al. 1992; Mercadier et al. 2011; Alexandre et al. 2015a, 2015b; Corcoran and Simonetti
419 2020). The chondrite-normalized REE patterns of uraninite from various occurrences, e.g., from
420 Shinkolobwe in the DR Congo; Orphan in Arizona, USA; Schwartzwalder in Colorado, USA;
421 Great Bear Lake in Canada; Morogoro in Tanzania; Roode pegmatite in Norway; and Jáchymov
422 in the Czech Republic show coinciding enrichment of MREE with a maximum at Gd or Tb
423 (Hidaka et al. 1992; Plášil et al. 2014; Alexandre et al. 2015a, 2015b; Balboni et al. 2017;
424 Corcoran and Simonetti 2020). In addition, most of the REE patterns of the aforementioned
425 common uraninites show an M-type tetrad effect with or without the Eu negative anomaly, which
426 is consistent with the REE pattern of uraninite I at Zimná Voda and linked with the non-
427 CHARAC behavior and genesis of uranium ore. Considering the occurrence of M-type tetrad
428 effect in the REE pattern of evolved granites-pegmatites and associated hydrothermal ore
429 deposits (Masuda et al. 1987; Irber 1999; Badanina et al. 2006; Peretyazhko and Savina 2010), it
430 is likely that hypogene uraninite I and particularly xenotime I show an inherited geochemical
431 signature of genetically-related Permian rare-metal Li–F granites of the Gemeric Unit, where the
432 whole-rock M-type tetrad effect and a high volatile flux is clearly documented (Broska and Kubiš
433 2018). The mechanism of the tetrad effect formation still remains unclear; however, it is
434 connected evidently to fluorine-controlled complexing in highly evolved ligand-rich
435 environments (e.g., Irber 1999; Masau et al. 2002; Veksler et al. 2005; Badanina et al. 2006;
436 Čopjaková et al. 2015).

437 The common, yet quantitatively variable presence of fluorapatite in all REE-U-(Au)-rich
438 quartz vein occurrences in the Gemeric Unit (Prakovce - Zimná Voda, Čučma - Majerská Valley,
439 Hnilec - Peklisko; Rojkovič et al. 1997, 1999; Števko et al. 2014; Ferenc et al. 2017; 2021; our
440 results) documents such a F-rich fluid environment. However, in Gd-dominant monazite with the
441 most pronounced W-type tetrad effect (Fig. 4e), a considerable depletion in La, Ce, and Pr, as
442 well as the enrichment of Sm and Gd seem to indicate a gradual development toward late-
443 crystallized mineral phases during low-temperature precipitation from aqueous fluids. Moreover,
444 the progressive flattening of pronounced M-type HREE pattern of xenotime I is clearly visible in
445 xenotime II and can also be attributed to late crystallization from aqueous fluids. Alternatively, or
446 even additionally, the potential source of P, Be and MREE-enrichment could be from
447 (meta)sedimentary host rocks associated with organic matter (cf. Kidder and Eddy-Dilek 1994;
448 Repina 2010; Franz et al. 2015).
449 In summary, the REE were released during the alteration of primary REE-bearing minerals,
450 the first generation of uraninite, brannerite, fluorapatite, monazite-(Ce), xenotime-(Y), and
451 hingganite-(Y). The REE budget shows the initial MREE-rich pattern that reflects the MREE-
452 selective behavior of altered minerals. The promoted crystallization of early monazite-(Ce)
453 selectively decreases the LREE content in the REE budget, whereas early crystallization of
454 xenotime I decreases the Y + HREE content. Since none of the MREE-selective minerals (e.g.,
455 young apatite, fluorite, titanite, and calcite) precipitate during this stage, the fluid becomes more
456 enriched in MREE and results in localized Gd±(MREE) predominance. However, this scenario is
457 likely only in an isochemical system; even local mass transport on a small spatial scale must
458 occur during precipitation. These findings suggest the localized process in a chemically near-
459 closed system where the circulation of fluids is limited. A similar scenario of core to rim (Y +

460 HREE)/LREE ratio development during garnet growth was described from A-type granite in the
461 Pre-Variscan Brno Batholith (Hönig et al. 2014).

462 One interesting aspect that emerged from our data is the clear connection of Gd (MREE)
463 enrichment with uranium ore and the subsequent alteration of uraninite and brannerite. The
464 genesis of lepersonnite-(Gd) is related to U-rich solutions and occurs in close proximity to altered
465 uraninite (cf. Finch and Ewing 1992). Likewise, the REE patterns for the Australian Proterozoic
466 U deposits (McLennan and Taylor 1979, Fisher et al. 2013) show a characteristic enrichment in
467 MREE and significant LREE depletion (cf. Franz et al. 2015). These data, along with our results,
468 suggest that the significant fractionation of REE with selective enrichment of MREE, particularly
469 Gd, can occur via alteration and leaching of uraninite ± fluorapatite ore by low-temperature, F-
470 rich aqueous fluids.

471

472 ## IMPLICATIONS

473 Lanthanoids represent essential elements of modern technology. Consequently, understanding
474 their behavior and precipitation conditions in natural systems, including MREE (Sm, Eu, Gd, Tb,
475 Dy), is crucial for their exploration and potential exploitation. This study focuses on a very
476 unusual assemblage of Gd (MREE)-rich minerals formed during the interaction of primary
477 minerals with low-*T* hydrothermal fluids. Such progressive development of Gd (MREE)
478 enrichment is a poorly-described process in nature. Nonetheless, the detailed microanalytical and
479 spectroscopic data, along with the microtextural observations reported here, provide evidence for
480 gradual remobilization-fractionation of U+REE in aqueous media. This study also demonstrated
481 the continuous evolution of the W-type tetrad effect from REE patterns without tetrad effect to
482 the well-developed W-type tetrad effect during the crystallization of monazite towards

483 Ce→Nd→Sm→Gd species. Similarly, the evolution from the REE patterns with well-developed
484 M-type tetrad effect to the patterns with less pronounced or no M-type tetrad effect is
485 documented during xenotime crystallization towards Y→Gd species. This clearly indicates that
486 the W-type tetrad effect gradually develops during progressive precipitation from the aqueous
487 media and associated processes, and thus the pattern gradates to the late and low-temperature
488 hydrothermal stage. The primary monazite-(Ce), xenotime-(Y), and hingganite-(Y) were partially
489 replaced by the assemblage of Gd-(MREE)-rich minerals during the interaction with F-rich
490 fluids. Middle REE generally do not comprise any mineral end-members and are considered to be
491 consistently present at low concentrations when compared to their LREE or HREE counterparts.
492 This study shows that low-*T* hydrothermal alteration and replacement reactions of MREE-
493 selective, but nominally REE-free minerals, e.g., uraninite, brannerite, and fluorapatite, can
494 produce an enhanced MREE signature in chemically-closed systems. Moreover, localized Gd-
495 rich environment remains an important direction for future research.

496 Finally, Gd-rich, and Gd-dominant minerals are quite rare in nature and thus of high
497 importance, since they often indicate extreme compositional regimes (e.g., Anenburg 2020). The
498 mineral with the composition of "monazite-(Gd)" reported here most likely represents the last
499 missing REE-dominant orthophosphate of the MGM in nature, since the other potential
500 lanthanoids Pr, Eu and Pm are three of the least abundant lanthanoids in the Earth's crust and
501 other Tb to Dy have ionic radii that are preferentially accommodated in the xenotime structure.
502 Moreover, our results show an existence of natural Gd-dominant xenotime, third member
503 together with xenotime-(Y) and xenotime-(Yb). Consequently, future investigation may complete
504 the list of already known members of MGM and XGM.
505

ACKNOWLEDGEMENTS

This work was supported by the Slovak Research and Development Agency under the contracts APVV-18-0065 and APVV-19-0065, VEGA Agency 1/0467/20 and by the European Regional Development Fund: ITMS 26220120064, ITMS 26210120024 and ITMS 26210120013. We thank Michael Sabo for reviewing the English content. Finally, we thank Michael Anenburg, Gerhard Franz (Reviewers), and Daniel Harlov (Associate Editor) for their constructive suggestions.

SUPPLEMENTARY MATERIAL

All Raman data, WDS scan of REE region (MGM) and a selection of EPMA analyses are available in the Supplementary material.

REFERENCES

Abedini, A., Rayaei Azizi, M., and Calagari, A.A. (2019) REE tetrad effect as a powerful indicator of formation conditions of karst bauxites: a case study of the Shahindezh Deposit, NW Iran. Acta Geologica Sinica, 93, 912–927.

Alexandre, P., Kyser, K., Layton-Matthews, D., Joy, B. (2015a) Chemical compositions of natural uraninite. Canadian Mineralogist, 53, 595–622.

Alexandre, P., Peterson, R., and Joy, B. (2015b) Sector zoning in uraninite. Canadian Mineralogist, 53, 1–11.

Åmli, R., and Griffin, W.L. (1975) Microprobe analysis of REE minerals using empirical correction factors. American Mineralogist, 60, 599–606.

Anenburg, M. (2020) Rare earth mineral diversity controlled by REE pattern shapes. Mineralogical Magazine, 84, 629–639.

529 Anenburg, M., Mavrogenes, J.A., and Bennett, V.C. (2020a) The Fluorapatite P–REE–Th Vein
530 Deposit at Nolans Bore: Genesis by Carbonatite Metasomatism. Journal of Petrology, 61,
531 egaa003.
532 Anenburg, M., Mavrogenes, J.A., Frigo, C., and Wall F. (2020b) Rare earth element mobility in
533 and around carbonatites controlled by sodium, potassium, and silica. Science Advances, 6,
534 eabb6570
535 Anenburg, M., and Williams, M.J. (2022) Quantifying the Tetrad Effect, Shape Components, and
536 Ce–Eu–Gd Anomalies in Rare Earth Element Patterns. Mathematical Geosciences, 54, 47–70.
537 Bačík, P., Miyawaki, R., Atencio, D., Cámara, F., and Fridrichová, J. (2017) Nomenclature of the
538 gadolinite supergroup. European Journal of Mineralogy, 29, 1067–1082.
539 Badanina, E.V., Trumbull, R.B., Dulski, P., Wiedenbeck, M., Veksler, I.V., and Syritso, L.F.
540 (2006) The behavior of rare-earth and lithophile trace elements in rare-metal granites: a study
541 of fluorite, melt inclusions and host rocks from the Khangilay complex, Transbaikalia, Russia.
542 Canadian Mineralogist, 44, 667–692.
543 Bajaník, Š., Hanzel, V., Mello, J., Pristaš, J., Reichwalder, P., Snopko, L., Vozár, J., and
544 Vozárová, A. (1983) Explanation to geological map of the Slovenské Rudohorie Mts. –
545 eastern part, 1:50 000, 223 p. State Geological Institute of D. Štúr, Bratislava (in Slovak).
546 Bajaník, Š., Ivanička, J., Mello, J., Reichwalder, P., Pristaš, J., Snopko, L., Vozár, J., and
547 Vozárová, A. (1984) Geological map of the Slovenské Rudohorie Mts. – eastern part, 1 :
548 50 000, 1st ed.; State Geological Institute of D. Štúr: Bratislava, Czechoslovakia (in Slovak).
549 Balboni, E., Simonetti, A., Spano, T., Cook, N.D., and Burn, P.C. (2017) Rare-earth element
550 fractionation in uranium ore and its U(VI) alteration minerals. Applied Geochemistry, 87, 84–
551 92.

552 Banfield, J.F., and Eggleton, R.A. (1989) Apatite replacement and rare earth mobilisation,
553 fractionation, and fixation during weathering. Clays and Clay Minerals, 37, 113–127.
554 Barrat, J.A., Zanda, B., Moynier, F., Bollinger, C., Liorzou, C., and Bayon, G. (2012)
555 Geochemistry of CI chondrites: Major and trace elements, and Cu and Zn Isotopes.
556 Geochimica et Cosmochimica Acta, 83, 79–92.
557 Boakye, E.E., Mogilevsky, P., Hay, R.S., and Fair, G.E. (2008) Synthesis and phase composition
558 of lanthanide phosphate nanoparticles $LnPO_4$ (Ln = La, Gd, Tb, Dy, Y) and solid solutions for
559 fiber coatings. Journal of the American Ceramic Society, 91, 3841–3849.
560 Bogatikov, O.A., Mokhov, A.V., Kartashov, P.M., Magazina, L.O., Koporulina, E.V.,
561 Ashikhmina, N.A., and Gorshkov, A.I. (2004) Selectively Gd-enriched micro- and nano-sized
562 minerals in the lunar regolith from the Crisium Mare. Doklady Akademii Nauk, 394, 81–84
563 (in Russian).
564 Braun, J.-J., Pagel, M., Muller, J.-P., Bilong, P., Michard, P., and Guillet, B. (1990) Cerium
565 anomalies in lateritic profile. Geochimica et Cosmochimica Acta, 54, 781–795.
566 Broska, I., and Kubiš, M., (2018) Accessory minerals and evolution of tin-bearing S-type granites
567 in the western segment of the Gemeric Unit (Western Carpathians). Geologica Carpathica, 69,
568 483–497.
569 Buck, H.M., Cooper, M.A., Černý, P., Grice, J.D., and Hawthorne, F.C. (1999) Xenotime-(Yb),
570 $YbPO_4$, a new mineral species from the Shatford Lake pegmatite group, southeastern
571 Manitoba, Canada. Canadian Mineralogist, 37, 1303–1306.
572 Clavier, N., Mesbah, A., Szenknect, S., and Dacheux, N. (2018) Monazite, rhabdophane,
573 xenotime and churchite: Vibrational spectroscopy of gadolinium phosphate polymorphs.
574 Spectrochimica Acta Part A: Molecular and Biomolecular Spectroscopy, 205, 85–94.

575 Clavier, N., Podor, R., and Dacheux, N. (2011) Crystal chemistry of the monazite structure.
576 Journal of the European Ceramic Society, 31, 941–976.
577 Corcoran, L., and Simonetti A. (2020) Geochronology of uraninite revisited. Minerals, 10, 205.
578 Čopjaková, R., Novák, M., and Franců, E. (2011) Formation of authigenic monazite-(Ce) to
579 monazite-(Nd) from Upper Carboniferous graywackes of the Drahany Upland: Roles of the
580 chemical composition of host rock and burial temperature. Lithos, 127, 373–385.
581 Čopjaková, R., Škoda, R., Vašinová Galiová, M., Novák, M., and Cempírek, J. (2015) Sc and
582 REE-rich tourmaline replaced by Sc-rich REE-bearing epidote-group mineral from the mixed
583 (NYF plus LCT) Kracovice pegmatite (Moldanubian Zone, Czech Republic). American
584 Mineralogist, 100, 1434–1451.
585 Deliens, M., and Piret, P. (1982) Bijvoetite et lepersonnite carbonates hydratés d'uranyle et des
586 terres rares de Shinkolobwe, Zaïre. Canadian Mineralogist, 20, 231–238 (in French).
587 Demartin, F., Pilati, T., Diella, V., Donzelli, S., Gentile, P., and Gramaccioli, C.M. (1991a) The
588 chemical composition of xenotime from fissures and pegmatites in the Alps. Canadian
589 Mineralogist, 29, 69–75.
590 Demartin, F., Pilati, T., Diella, V., Donzelli, S., and Gramaccioli, C.M. (1991b) Alpine monazite:
591 further data. Canadian Mineralogist, 29, 61–67.
592 Demartin, F., Pilati, T., Diella, V., Gentile, P., and Gramaccioli, C.M. (1993) A crystal-chemical
593 investigation of Alpine gadolinite. Canadian Mineralogist, 30, 127–136.
594 Donát, A., Miháľ, F., and Novotný, L. (2000) Geological survey works on Au in the Older
595 Paleozoic in SGR, 209 p. Manuscript, State Geological Institute of D. Štúr archive, Bratislava
596 (in Slovak)

597 Dowman, E., Wall, F., Treloar, P.J., and Rankin, A.H. (2017) Rare-earth mobility as a result of
598 multiple phases of fluid activity in fenite around the Chilwa Island Carbonatite, Malawi.
599 Mineralogical Magazine, 81, 1367–1395.
600 Faryad, S.W. (1991) Metamorphism of the Early Paleozoic sedimentary rocks in Gemericum.
601 Mineralia Slovaca, 23, 315–324 (in Slovak).
602 Ferenc, Š., Biroň, A., Sejkora, J., and Sýkorová, M. (2017) Phosphuranylite from the oxidation
603 zone of the vein quartz-apatite-REE-U mineralization at Majerská Valley near Čučma
604 (Slovenské Rudohorie Mts., Gemeric Unit. Bulletin Mineralogie Petrologie, 25, 23–32.
605 Ferenc, Š., Števko, M., Mikuš, T., Milovská S., Kopáčik R., and Hoppanová E. (2021) Primary
606 minerals and age of the hydrothermal quartz veins containing U-Mo-(Pb, Bi, Te)
607 mineralization in the Majerská Valley near Čučma (Gemeric Unit, Spišsko-gemerské
608 rudohorie Mts., Slovak Republic). Minerals, 11, 629.
609 Finch, R.J., and Ewing, R.C. (1992) The corrosion of uraninite under oxidizing conditions.
610 Journal of Nuclear Materials, 190, 133–156.
611 Fisher, L.A., Cleverley, J.S., and Pownceby, M. (2013) 3D representation of geochemical data,
612 the corresponding alteration and associated REE mobility at the Ranger uranium deposit,
613 Northern Territory, Australia. Mineralium Deposita, 48, 947–966.
614 Fisher, F.G., and Meyrowitz, R. (1962) Brockite, a new calcium thorium phosphate from the Wet
615 Mountains, Colorado. American Mineralogist, 47, 1346–1355.
616 Förster, H.-J. (1998a) The chemical composition of REE–Y–Th–U rich accessory minerals from
617 the Erzgebirge–Fichtelgebirge region, Germany. Part I: the monazite-(Ce) – brabantite solid
618 solution series. American Mineralogist, 83, 259–272.

619 Förster, H.-J. (1998b) The chemical composition of REE–Y–Th–U-rich accessory minerals in
620 peraluminous granites of the Erzgebirge–Fichtelgebirge region, Germany. Part II: xenotime.
621 American Mineralogist, 83, 1302–1315.
622 Förster, H.-J., and Rhede, D. (1995) Composition of monazite and xenotime from the
623 Fichtelgebirge granites – an electron microprobe study. Berichte der Deutschen
624 Mineralogischen Gesellschaft, Beihefte zum European Journal of Mineralogy, 7, 68.
625 Franz, G., Morteani, G., and Rhede, D. (2015) Xenotime‐(Y) formation from zircon dissolution–
626 precipitation and HREE fractionation: an example from a metamorphosed phosphatic
627 sandstone, Espinhaço fold belt (Brazil). Contribution to Mineralogy and Petrology, 170, 37.
628 Graeser, S., and Schwander, H. (1987) Gasparite-(Ce) and monazite-(Nd): two new minerals to
629 the monazite group from the Alps. Schweizerische Mineralogische und Petrographische
630 Mitteilungen, 67, 103–113.
631 Gratz, R., and Heinrich, W. (1998) Monazite-xenotime thermometry. III. Experimental
632 calibration of the partitioning of gadolinium between monazite and xenotime. European
633 Journal of Mineralogy, 10, 579–588.
634 Grawunder, A., Merten, D., and Büchel, G. (2014) Origin of middle rare earth element
635 enrichment in acid mine drainage-impacted areas. Environmental Science and Pollution
636 Research, 21, 6812–6823.
637 Hannigan, R.E., and Sholkowitz, E.R. (2001) The development of middle rare earth element
638 enrichments in freshwaters: weathering of phosphate minerals. Chemical Geology, 175, 495–
639 508.
640 Hay, R.S., Mogilevsky, P., and Boakye, E. (2013) Phase transformations in xenotime rare-earth
641 orthophosphates. Acta Materialia, 61, 6933–6947.

642 Hazen, R.M., Hystad, G., Downs, R.T., Golden, J.J., Pires, A.J., and Grew, E.S. (2015) Earth's
643 "missing" minerals. American Mineralogist, 100, 2344–2347.
644 Heuser, J., Bukaemskiy, A.A., Neumeier S., Neumann A., and Bosbach, D., (2014) Raman and
645 infrared spectroscopy of monazite-type ceramics used for nuclear waste conditioning. Progress
646 in Nuclear Energy, 72, 149–155.
647 Hidaka, H., Holliger, P., Shimizu, H., and Masuda, A. (1992) Lanthanide tetrad effect observed
648 in the Oklo and ordinary uraninites and its implication for their forming processes.
649 Geochemical Journal, 26, 337–346.
650 Hönig, S., Čopjaková, R., Škoda, R., Novák, M., Dolejš, D., Leichmann, J., and Vašinová
651 Galiová, M. (2014) Garnet as a major carrier of the Y and REE in the granitic rocks: An
652 example from the layered anorogenic granite in the Brno Batholith, Czech Republic. American
653 Mineralogist, 99, 1922–1941.
654 Huittinen, N., Arinicheva, Y., Kowalski, P., Vinograd, V., Neumeier, S., and Bosbach, D. (2017).
655 Probing structural homogeneity of La1−xGdxPO$_4$ monazite-type solid solutions by combined
656 spectroscopic and computational studies. Journal of Nuclear Material, 486, 148–157.
657 Irber, W. (1999) The lanthanide tetrad effect and its correlation with K/ Rb, Eu/Eu*, Sr/Eu,
658 Y/Ho, and Zr/Hf of evolving peraluminous granite suites. Geochimica et Cosmochimica Acta,
659 63, 489–508.
660 Ivanička, J., Snopko, L., Snopková, P., and Vozárová, A. (1989) Gelnica Group – Lower Unit of
661 Spišsko-Gemerské Rudohorie Mts. (West Carpathians), Early Paleozoic. Geologica
662 Carpathica, 40, 483–501.

Kidder, D.L., and Eddy-Dilek, C.A. (1994) Rare-earth element variation in phosphate nodules from midcontinent Pennsylvanian cyclothems. Journal of Sedimentary Research, A64, 584–592.

Kolitsch, U., and Holtstam, D. (2004) Crystal chemistry of $REEXO_4$ compounds (X = P, As,V). II. Review of $REEXO_4$ compounds and their stability fields. European Journal of Mineralogy, 16, 117–126.

Krneta, S., Ciobanu, C.L., Cook, N.J., Ehrig, K., and Kontonikas-Charos, A. (2017) Rare earth element behavior in apatite from the Olympic Dam Cu/U/Au/Ag deposit, South Australia. Minerals, 7, 135.

Lee, S.G., Asahara, Y., Tanaka, T., Lee, S.R., and Lee, T. (2013) Geochemical significance of the Rb-Sr, La-Ce and Sm-Nd isotope systems in A-type rocks with REE tetrad patterns and negative Eu and Ce anomalies: The Cretaceous Muamsa and Weolaksan granites, South Korea. Chemie der Erde, 73, 75–88.

Lenz, Ch., Nasdala, L., Talla, D., Hauzenberger, Ch., Seitz, R., Kolitsch, U. (2015) Laser-induced REE^{3+} photoluminescence of selected accessory minerals — An "advantageous artefact" in Raman spectroscopy. Chemical Geology, 415, 1–16.

Li, W., Ding, X., Meng, Ch., Ren, Ch., Wu, H., and Yang, H. (2018) Phase structure evolution and chemical durability studies of $Gd_{12x}Yb_xPO_4$ ceramics for immobilization of minor actinides. The Journal of Materials Science, 53, 6366–6377.

Lösch, H., Hirsch, A., Holthausen, J., Peters, L, Xiao, B., Neumeier, S., Schmidt, M., and Huittinen, N. (2019) A spectroscopic investigation of Eu^{3+} incorporation in $LnPO_4$ (Ln = Tb, $Gd_{1-x}Lu_x$, X = 0.3, 0.5, 0.7, 1) ceramics. Frontiers in Chemistry, 7, 94

MacDonald, R., Bagiński, B., Kartashov, P.M., Zozulya, D., and Dzierzanowski, P. (2015) Interaction of rare-metal minerals with hydrothermal fluids; evidence from quartz-epidote metasomatites of the Haldzan Buragtag massif, Mongolian Altai. Canadian Mineralogist, 53, 1015–1034.

Maftei, A.E., Buzatu, A., Damian, G., Buzgar, N., Dill, H.G., and Apopei, A.I. (2020) Micro-Raman—a tool for the heavy mineral analysis of gold placer-type deposits (Pianu Valley, Romania). Minerals, 10, 988.

Massau, M., Černý, P., and Chapman, R. (2000) Dysprosian xenotime-(Y) from the Annie Claim #3 granitic pegmatite, Southeastern Manitoba, Canada: Evidence of the tetrad effect? Canadian Mineralogist, 38, 899–905.

Massau, M., Černý, P., Cooper, M.A., Chapman, R., and Grice, J.D. (2002) Monazite-(Sm), a new member of the monazite group from the Annie Claim #3 granitic pegmatite, Southeastern Manitoba. Canadian Mineralogist, 40, 1649–1655.

Masuda, A., Kawakami, O., Dohmoto, Y., and Takenaka, T. (1987) Lanthanide tetrad effects in nature: two mutually opposite types, W and M. Geochemical Journal, 21, 119–124.

Mayer, B.S., Krenn, E., and Finger, F. (2014) Microcrystals of Th-rich monazite (La) with a negative Ce anomaly in metadiorite and their role for documenting Cretaceous metamorphism in the Slavonian Mountains (Croatia). Mineralogy and Petrology, 108, 231–243.

McLennan, S.M., and Taylor, S.R. (1979) Rare earth element mobility associated with uranium mineralization. Nature, 282, 247–249.

Meng, Ch., Ding, X., Zhao, J., Ren, Ch., Fu, H., and Yang, H. (2016) Phase evolution and microstructural studies of $Gd_{1-x}Yb_xPO_4$ ($0 \leq x \leq 1$) ceramics for radioactive waste storage. Journal of the European Ceramic Society, 36, 773–779.

Mercadier, J., Cuney, M., Lach, P., Boiron, M.C., Bonhoure, J., Richard, A., Leisen, M., and Kister, P. (2011) Origin of uranium deposits revealed by their rare earth element signature. Terra Nova, 23, 264–269.

Migdisov, A., Guo, X., Nisbet, H., Xu, H., and Williams-Jones, A.E. (2019) Fractionation of REE, U, and Th in natural ore-forming hydrothermal systems: Thermodynamic modeling. Journal of Chemical Thermodynamics, 128, 305–319.

Minami, M., and Masuda, A. (1997) Approximate estimation of the degree of lanthanide tetrad effect from the data potentially involving all lanthanides. Geochemical Journal, 31, 125–133.

Mokhov, A.V., Kartashov, P.M., Gornostaeva, T.A., Bogatikov, O.A., and Ashikhmina, T.A. (2011) New phases of lanthanoids and actinoids from the regolith samples delivered by the Luna-24. Doklady Earth Sciences, 437, 479–482.

Morgan, B., Rate, A.W., Burton, E.D., and Smirk, M.N. (2012) Enrichment and fractionation of rare earth elements in FeS- and organic-rich estuarine sediments receiving acid sulfate soil drainage. Chemical Geology, 308–309, 60–73.

Mullica, D.F., Grossie, D.A., and Boatner, L.A. (1986) Crystal structure of 1:1 gadolinium/ytterbium orthophosphate. Inorganica Chimica Acta, 118, 173–176.

Mullica, D.F., Sappenfield, E.L., and Boatner, L.A. (1990) A structural investigation of several mixed lanthanide-orthophosphates. Inorganica Chimica Acta, 174, 155–159.

Muñoz, A., and Rodríguez-Hernández, P. (2018) High-pressure elastic, vibrational and structural study of monazite-type $GdPO_4$ from ab initio simulations. Crystals, 8, 209.

Ni, Y., Hughes, J.M., and Mariano, A.N. (1995) Crystal chemistry of the monazite and xenotime structures. American Mineralogist, 80, 21–26.

730 Ondrejka, M., Bačík, P., Sobocký, T., Uher, P., Škoda, R., Mikuš, T., Luptáková, J., and
731 Konečný, P. (2018) Minerals of the rhabdophane group and the alunite supergroup in
732 microgranite: products of low temperature alteration in a highly acidic environment from the
733 Velence Hills, Hungary. Mineralogical Magazine, 82, 1277–1300.
734 Ondrejka, M., Uher, P., Pršek, J., Ozdín, D. (2007) Arsenian monazite-(Ce) and xenotime- (Y),
735 REE arsenates and carbonates from the Tisovec-Rejkovo rhyolite, Western Carpathians,
736 Slovakia: composition and substitutions in the (REE, Y)XO_4 system (X = P, As, Si, Nb, S).
737 Lithos, 95, 116–129.
738 Pasero, M., Kampf, A.R., Ferraris, C., Pekov, I.V., Rakovan, J., and White, T.J. (2010)
739 Nomenclature of the apatite supergroup minerals. European Journal of Mineralogy, 22, 163–
740 179.
741 Pekov, I.V. (2000) Lovozero Massif, 480 p. Ocean Pictures Ltd., Moscow.
742 Peretyazhko, I.S., and Savina, E.A. (2010) Tetrad effects in the rare earth elements patterns of
743 granitoid rocks as an indicator of fluoride-silicate liquid immiscibility in magmatic systems.
744 Petrology, 18, 514–543.
745 Plášil, J., Sejkora, J., Škoda, R., and Škácha, P. (2014) The recent weathering of uraninite from
746 the Červená vein, Jáchymov (Czech Republic): a fingerprint of the primary mineralization
747 geochemistry onto the alteration association. Journal of Geosciences, 59, 223–253.
748 Rezaei Azizi, M., Abedini, A., and Alipour, S. (2017) Application of lanthanides tetrad effect as a
749 geochemical indicator to identify fluorite generations: A case study from the Laal-Kan fluorite
750 deposit, NW Iran. Comptes Rendus Géoscience Sciences de la Planète, 352, 43–58.
751 Repina, S.A. (2010) Zoning and sectoriality of the florencite and xenotime group minerals from
752 quartz veins, the Subpolar Urals. Geology of Ore Deposits, 52, 821–836.

753 Repina, S.A. (2011) Fractionation of REE in the xenotime and florencite paragenetic association
754 from Au–REE mineral occurrences of the Nether-Polar Urals. Geochemistry International, 49,
755 868–887.
756 Repina, S.A. (2014) Microheterogeneity of crystal growth zones as a result of REE fractionation.
757 Geochemistry International, 52, 1057–1071.
758 Rodriguzez-Liviano, S., Becerro, A.I., Alcántara, D., Grazú, V., de la Fuente, J.M., and Ocaña,
759 M. (2013) Synthesis and properties of multifunctional tetragonal Eu: $GdPO_4$ nanocubes for
760 optical and magnetic resonance imaging applications. Inorganic Chemistry, 52, 647–654.
761 Rojkovič, I., Háber, M., and Novotný, L. (1997) U-Au-Co-Bi-REE mineralization in the Gemeric
762 unit (Western Carpathians, Slovakia), Geologica Carpathica, 48, 303–313.
763 Rojkovič, I., Konečný, P., Novotný, L., Puškelová, Ľ., and Streško, V. (1999) Quartz-apatite-
764 REE vein mineralization in Early Paleozoic rocks of the Gemeric Superunit, Slovakia.
765 Geologica Carpathica, 50, 215–227.
766 Ruschel, K., Nasdala, L., Kronz, A., Hanchar, J.M., Többens, D.M., Škoda, R., Finger, F., and
767 Möller, A. 2012 A Raman spectroscopic study on the structural disorder of monazite–(Ce).
768 Mineralogy and Petrology, 105, 41–55.
769 Schandl, E.S., and Gorton, M.P. (2004) A textural and geochemical guide to the identification of
770 hydrothermal monazite: Criteria for selection of samples for dating epigenetic hydrothermal
771 ore deposits. Economic Geology, 99, 1027–1035.
772 Seredin, V.V. (1996) Rare earth element-bearing coals from the Russian Far East deposits.
773 International Journal of Coal Geology, 30, 101–129.
774 Shannon, R.D. (1976) Revised effective ionic radii and systematic studies of interatomic
775 distances in halides and chalcogenides. Acta Crystallographica, A32, 751–767.

776 Števko, M., Uher, P., Ondrejka, M., Ozdín, D., and Bačík, P. (2014) Quartz–apatite–REE
777 phosphates–uraninite vein mineralization near Čučma (eastern Slovakia): a product of early
778 Alpine hydrothermal activity in the Gemeric Superunit, Western Carpathians. Journal of
779 Geosciences, 59, 209–222.
780 Takahashi, Y., Hidekazu, Y., Sato, N., Hama, K., Yusa, Y., and Shimizu, H. (2002) W- and M-
781 type tetrad effects in REE patterns for water–rock systems in the Tono uranium deposit,
782 central Japan. Chemical Geology, 184, 311–335.
783 Veksler, I.V., Dorfman, A.M., Kamenetsky, M., Dulski, P., and Dingwell, D.B. (2005)
784 Partitioning of lanthanides and Y between immiscible silicate and fluoride melts, fluorite and
785 cryolite and the origin of the lanthanide tetrad effect in igneous rocks. Geochimica et
786 Cosmochimica Acta, 69, 2847–2860.
787 Villaseñor, G., Catlos, E.J., Broska, I., Kohút, M., Hraško, Ľ., Aguilera, K., Etzel, T.M., Kyle, R.,
788 and Stockli, D.F. (2021) Evidence for widespread mid-Permian magmatic activity related to
789 rifting following the Variscan orogeny (Western Carpathians). Lithos, 390-391, 106083.
790 Vozárová, A., Šarinová, K., Sergeev, S., Larionov, A., and Presnyakov, S. (2010) Late
791 Cambrian/Ordovician magmatic arc type volcanism in the Southern Gemericum basement,
792 Western Carpathians, Slovakia: U–Pb (SHRIMP) data from zircons. International Journal of
793 Earth Sciences, 99, 17–37.
794 Zhao, Z.H., Bao, Z.W., and Qiao, Y.L. (2010) A peculiar composite M- and W-type REE tetrad
795 effect: Evidence from the Shuiquangou alkaline syenite complex, Hebei Province, China.
796 Chinese Science Bulletin, 55, 2684−2696.

797

798 **Figure captions**

799

800 **FIGURE 1. (a)** Simplified geological-tectonic sketch-map of the Western Carpathians. **(b)** A
801 geological map of the studied area (modified after Bajaník et al. 1984). **(c)** A close-up view on
802 the veins, alteration and host rocks (modified after Donát et al. 2000).

803

804 **FIGURE 2.** BSE images of uraninite + brannerite textures and generations and flurorapatite from
805 the Zimná Voda REE-U-Au mineralization. (**a**) Large botryoidal aggregates of uraninite I (Urn I)
806 with globular microstructure showing numerous desiccation cracks and cavities filled with
807 brannerite I (Bnr I). Uraninite II (Urn II) forms altered rim around uraninite I. Newly-formed
808 uraninite III (Urn III) forms scattered crystals in the proximity of Urn I. Other secondary minerals
809 are uranyl arsenates-phosphates (U-As-P). (**b**) Fractured uraninite I (Urn I) with altered rim of
810 uraninite II (Urn II) in association with gersdorffite (Gdf) and quartz (Qz). (**c**) Fractured globular
811 uraninite I (Urn I) with altered inner domains (Urn II) in quartz (Qz). (**d**) Globular aggregate of
812 uraninite I (Urn I) and its secondary generations consisting of altered rim, inner altered domains
813 (Urn II), and newly-formed crystals (Urn III), associated with secondary uranyl arsenates-
814 phosphates (U-As-P) and quartz (Qz). (**e**) Large aggregates of brannerite I (Bnr I) in association
815 with gold (Au), uraninite I (Urn I) and uranyl arsenates-phosphates (U-As-P). (**f**) Large
816 aggregates of brannerite I (Bnr I), altered domains of brannerite II (Bnr II) associated with
817 uraninite I (Urn I) and quartz (Qz). (**g**) Primary fluorapatite (Fap) scattered in quartz (Qz) and
818 muscovite (Ms). Other minerals are xenotime-(Y) (Xtm), uraninite III (Urn III), and
819 pharmacosiderite (Pmsd).

820

FIGURE 3. (**a, d**) BSE images and false color X-ray mapping showing the distribution of chemical elements in uraninite aggregate (**b**–**c**), MGM–xenotime-(Y) (**e**–**o**) and hingganite-(Y) **(p-r)**. Images **j–o** are the same as rotated Fig. 5g and images **r–s** are the same as Fig. 5h.

FIGURE 4. Fitted chondrite-normalized REE patterns of minerals from sample ZV-2. Tetrad effect parameters according to Minami and Masuda (1997). Chondrite values are from Barrat et al. (2012).

FIGURE 5. BSE images of REE minerals from the Zimná voda REE-U-Au mineralization. (**a**) Compositionally-heterogeneous aggregate of xenotime I (Xtm I) and remobilized Gd-rich xenotime II (Xtm II) associated with monazite-(Ce) (Mnz-Ce) and uraninite (Urn) in quartz-muscovite gangue (Qz + Ms). (**b**) Xenotime I (Xtm I) with marginal domains rich in Gd (Xtm II) with monazite-(Nd) (Mnz-Nd) and monazite-(Sm) (Mnz-Sm). (**c**) Monazite-(Nd) (Mnz-Nd) in association with xenotime I (Xtm I) with rims of Gd-rich xenotime II (Xtm II) and numerous inclusions of uraninite (Urn) in quartz (Qz). (**d**) Heterogeneous aggregate of monazite-(Sm) (Mnz-Sm) and "monazite-(Gd)" (Mnz-Gd) with xenotime I (Xtm I), Gd-rich xenotime II (Xtm II) and uranyl arsenates-phosphates (U-As-P) in quartz-muscovite gangue (Qz + Ms). (**e**) Large and compositionally-heterogeneous aggregate of xenotime I + II (Xtm I + II) with numerous inclusions of uranyl arsenates-phosphates (U-As-P) in quartz (Qz). (**f**) Monazite-(Nd) (Mnz-Nd) and xenotime I with Gd-rich xenotime II outer domains (Xtm II) in quartz (Qz) associated with uranyl arsenates-phosphates (U-As-P). (**g**) Heterogeneous aggregate of xenotime I (Xtm I) penetrated by xenotime II vein (Xtm II) in association with uranyl arsenates-phosphates (U-As-P)

in scorodite (Scd) and quartz (Qz). (**h**) Cracked crystal of hingganite I (Hin I) with Gd-rich domains of hingganite II (Hin II) in quartz (Qz) gangue.

FIGURE 6. Composition of monazite- and xenotime-group minerals in ternary LREE-MREE-HREE diagram (atomic proportions).

FIGURE 7. Composition of xenotime-group minerals in ternary Dy-Gd-Y diagram (atomic proportions).

FIGURE 8. Quadrilateral compositional diagram of the gadolinite-group minerals (Bačík et al. 2017) with positions of hingganite-(Y).

Table captions

TABLE 1. Representative EPMA analyses and mineral formulae. *Note*: n.a. = not analyzed; int. = interior; recalc = recalculated. Urn = uraninite; Bnr = brannerite; Fap = fluorapatite; Mnz = monazite; Xtm = xenotime; Hin = hingganite.

TABLE 1. Representative EPMA analyses and mineral formulae.

(wt%)	Urn I	Urn II rim	Urn II int.	Urn III		Bnr I	Bnr II		Fap		Mnz Ce	Mnz Nd	Mnz Sm	Mnz "Gd"	Mnz "Gd"	Xtm I Y	Xtm II "Gd"		Hin I Y	Hin II Y
SO_3	0.03	0.00	0.04	0.00	WO_3	1.04	3.68	SO_3	0.00	SO_3	0.02	0.01	0.01	0.00	0.00	n.a.	n.a.	P_2O_5	0.04	0.07
WO_3	1.62	0.60	9.33	0.04	$UO_{3recalc}$	17.38	35.17	P_2O_5	41.75	P_2O_5	28.97	30.06	30.30	29.98	29.46	33.64	29.73	As_2O_5	0.23	2.00
MoO_3	n.a.	n.a.	n.a.	0.00	Sb_2O_5	0.22	0.90	As_2O_5	0.00	As_2O_5	0.00	0.23	0.00	0.23	0.07	0.15	2.28	SiO_2	24.57	23.14
P_2O_5	0.19	0.06	0.25	0.00	Nb_2O_5	0.32	0.68	V_2O_5	0.01	SiO_2	0.58	0.02	0.18	0.17	0.03	0.32	0.17	ThO_2	0.00	n.a.
As_2O_5	0.70	0.19	0.59	0.00	TiO_2	35.44	29.09	SiO_2	0.04	ThO_2	0.30	0.00	0.00	0.02	0.00	0.02	0.00	UO_2	0.10	0.00
Sb_2O_5	n.a.	n.a.	n.a.	0.19	SiO_2	0.33	4.26	TiO_2	0.01	UO_2	0.03	0.02	0.04	0.00	0.06	1.14	0.56	B_2O_{3calc}	0.82	1.61
SiO_2	0.19	0.11	0.00	0.00	ThO_2	0.29	0.23	ThO_2	0.00	Al_2O_3	0.00	0.00	0.00	0.00	0.02	0.00	0.00	Bi_2O_3	n.a.	0.03
ThO_2	0.00	0.00	n.a.	0.00	$UO_{2recalc}$	38.48	4.31	UO_2	0.00	Y_2O_3	0.69	0.66	0.49	1.48	1.23	34.95	15.84	Al_2O_3	0.00	n.a.
UO_2	87.70	90.86	77.59	91.41	Bi_2O_3	0.00	0.00	Al_2O_3	0.00	La_2O_3	6.34	7.37	6.08	3.28	3.01	0.00	0.02	Y_2O_3	30.90	16.06
Al_2O_3	0.12	0.00	0.00	0.03	Al_2O_3	0.10	0.42	Y_2O_3	0.07	Ce_2O_3	15.91	15.04	11.87	6.73	6.88	0.00	0.07	La_2O_3	0.00	0.00
Y_2O_3	0.88	2.29	n.a.	2.51	Y_2O_3	0.29	2.05	La_2O_3	0.00	Pr_2O_3	2.61	2.37	1.96	1.15	1.11	0.03	0.05	Ce_2O_3	0.08	0.33
La_2O_3	0.12	0.00	n.a.	0.01	La_2O_3	0.08	0.00	Ce_2O_3	0.01	Nd_2O_3	15.68	15.63	14.36	9.76	10.62	0.47	0.40	Pr_2O_3	0.00	0.02
Ce_2O_3	0.22	0.05	n.a.	0.00	Ce_2O_3	0.16	0.19	Pr_2O_3	0.04	Sm_2O_3	14.90	14.51	17.32	17.68	17.45	2.43	5.77	Nd_2O_3	0.12	1.94
Pr_2O_3	0.12	0.13	n.a.	0.08	Pr_2O_3	0.00	0.00	Nd_2O_3	0.01	Eu_2O_3	0.30	0.04	1.61	1.59	1.62	0.85	1.34	Sm_2O_3	0.61	7.67
Nd_2O_3	0.15	0.00	n.a.	0.01	Nd_2O_3	0.21	0.71	Sm_2O_3	0.09	Gd_2O_3	9.97	11.15	13.23	22.74	23.36	8.42	28.67	Eu_2O_3	0.05	0.56
Sm_2O_3	0.34	0.17	n.a.	0.42	Sm_2O_3	0.17	1.13	Eu_2O_3	0.05	Tb_2O_3	0.66	0.73	0.59	1.50	1.58	1.56	3.78	Gd_2O_3	3.65	15.79
Eu_2O_3	0.12	0.20	n.a.	0.17	Eu_2O_3	0.00	0.16	Gd_2O_3	0.08	Dy_2O_3	1.18	1.00	0.93	2.49	2.31	8.07	10.56	Tb_2O_3	1.34	2.27
Gd_2O_3	0.65	0.50	n.a.	0.00	Gd_2O_3	0.00	1.73	Tb_2O_3	0.00	Ho_2O_3	0.04	0.46	0.10	0.24	0.20	0.86	0.45	Dy_2O_3	9.12	8.52
Tb_2O_3	0.22	0.21	n.a.	1.09	Tb_2O_3	0.05	0.22	Dy_2O_3	0.12	Er_2O_3	0.23	0.09	0.17	0.27	0.10	3.43	0.69	Ho_2O_3	1.42	0.80
Dy_2O_3	0.41	0.81	n.a.	0.60	Dy_2O_3	0.06	1.37	Ho_2O_3	0.03	Tm_2O_3	0.04	0.01	0.05	0.02	0.01	0.80	0.09	Er_2O_3	3.13	1.38
Ho_2O_3	0.11	0.06	n.a.	0.00	Ho_2O_3	0.00	0.12	Er_2O_3	0.03	Yb_2O_3	0.15	0.27	0.17	0.23	0.35	2.86	0.37	Tm_2O_3	0.31	1.17
Er_2O_3	0.26	0.87	n.a.	n.a.	Er_2O_3	0.06	0.29	Tm_2O_3	0.03	Lu_2O_3	0.10	0.00	0.03	0.01	0.02	0.36	0.05	Yb_2O_3	1.90	0.57
Tm_2O_3	0.04	0.07	n.a.	n.a.	Tm_2O_3	0.01	0.13	Yb_2O_3	0.00	CaO	0.32	0.29	0.16	0.49	0.10	0.07	0.01	Lu_2O_3	0.94	0.64
Yb_2O_3	0.03	0.52	n.a.	n.a.	Yb_2O_3	0.00	0.33	Lu_2O_3	0.02	SrO	0.07	n.a.	0.04	n.a.	n.a.	n.a.	n.a.	BeO_{calc}	9.70	8.94
Lu_2O_3	0.10	0.02	n.a.	n.a.	Lu_2O_3	0.04	0.04	CaO	54.69	FeO_{total}	0.08	0.03	0.08	0.16	0.03	0.03	0.00	FeO	7.22	1.89
CaO	0.47	0.05	0.43	0.00	$Fe_2O_{3\ total}$	0.88	1.74	SrO	0.00	PbO	0.00	0.00	0.00	0.03	0.00	0.02	0.03	MnO	0.00	0.02
SrO	0.00	0.00	0.27	0.00	MnO	0.09	0.21	BaO	0.00	MnO	0.02	0.07	0.06	0.00	0.04	n.a.	n.a.	CaO	0.59	0.67
FeO_{total}	0.23	0.00	0.72	0.00	MgO	0.05	0.00	PbO	0.00	F	0.00	n.a.	0.00	n.a.	n.a.	n.a.	n.a.	BaO	n.a.	0.28
PbO	2.72	1.87	0.71	1.53	CaO	1.36	1.88	MnO	0.05	Cl	0.05	0.03	0.02	0.02	0.04	n.a.	n.a.	F	n.a.	0.00
K_2O	n.a.	n.a.	1.13	0.09	SrO	0.07	0.10	FeO_{total}	0.01	O=F	0.00	0.00	0.00	0.00	0.00	0.00	0.00	H_2O_{calc}	1.88	3.16
Total	97.74	99.65	91.07	98.18	PbO	0.75	0.14	H_2O_{calc}	0.00	O=Cl	-0.01	-0.01	-0.01	-0.01	-0.01	0.00	0.00	Total	98.73	99.49
					K_2O	0.13	0.09	F	3.81	Total	99.24	100.07	99.84	100.27	99.68	100.46	100.93			
					Total	98.01	91.34	Cl	0.05											
								O=F	-1.61											
								O=Cl	-0.01											
								Total	99.40											

(apfu)	Urn I	Urn II	Urn II	Urn III		Bnr I	Bnr II		Fap		Mnz Ce	Mnz Nd	Mnz Sm	Mnz "Gd"	Mnz "Gd"	Xtm I Y	Xtm II "Gd"		Hin I Y	Hin II Y
S^{6+}	0.001	0.000	0.001	0.000	W^{6+}	0.019	0.066	S^{6+}	0.000	S^{6+}	0.001	0.000	0.000	0.000	0.000	-	-	Th^{4+}	0.000	-
W^{6+}	0.017	0.007	0.063	0.000	Sb^{5+}	0.006	0.023	P^{5+}	3.002	P^{5+}	0.981	1.005	1.012	1.006	1.005	0.986	0.957	U^{4+}	0.003	0.000
Mo^{6+}	-	-	-	0.000	Nb^{5+}	0.010	0.021	As^{5+}	0.000	As^{5+}	0.000	0.005	0.000	0.005	0.001	0.003	0.045	Bi^{3+}	-	0.005
P^{5+}	0.006	0.002	0.006	0.000	Ti^{4+}	1.861	1.507	V^{5+}	0.001	Si^{4+}	0.023	0.001	0.007	0.007	0.001	0.011	0.006	Y^{3+}	1.176	0.705
As^{5+}	0.015	0.004	0.008	0.000	Si^{4+}	0.023	0.293	Si^{4+}	0.004	Total X	1.005	1.011	1.020	1.017	1.008	1.000	1.009	La^{3+}	0.001	0.000
Sb^{5+}	-	-	-	0.000	Al^{3+}	0.008	0.034	Total T	3.007	Th^{4+}	0.003	0.000	0.000	0.000	0.000	0.000	0.000	Ce^{3+}	0.002	0.010
Si^{4+}	0.008	0.005	0.000	0.000	Fe^{3+}	0.046	0.09	Ti^{4+}	0.001	U^{4+}	0.000	0.000	0.000	0.000	0.001	0.009	0.005	Pr^{3+}	0.000	0.001
Th^{4+}	0.000	0.000	-	0.000	Total B	1.973	2.035	Th^{4+}	0.000	Al^{3+}	0.000	0.000	0.000	0.000	0.001	0.000	0.000	Nd^{3+}	0.006	0.057
U^{4+}	0.777	0.858	0.451	0.896	U^{6+}_{recalc}	0.255	0.509	U^{4+}	0.000	Y^{3+}	0.015	0.014	0.010	0.031	0.026	0.644	0.321	Sm^{3+}	0.036	0.218
Al^{3+}	0.005	0.000	0.000	0.001	Th^{4+}	0.005	0.004	Al^{3+}	0.000	La^{3+}	0.094	0.107	0.089	0.048	0.045	0.000	0.000	Eu^{3+}	0.005	0.016
Y^{3+}	0.019	0.052	-	0.059	U^{4+}_{recalc}	0.598	0.066	Y^{3+}	0.003	Ce^{3+}	0.233	0.217	0.171	0.098	0.102	0.000	0.001	Gd^{3+}	0.177	0.432
La^{3+}	0.002	0.000	-	0.000	Bi^{3+}	0.000	0.000	La^{3+}	0.000	Pr^{3+}	0.038	0.034	0.028	0.017	0.016	0.000	0.001	Tb^{3+}	0.049	0.061
Ce^{3+}	0.003	0.001	-	0.000	Y^{3+}	0.011	0.075	Ce^{3+}	0.000	Nd^{3+}	0.224	0.220	0.202	0.138	0.153	0.006	0.005	Dy^{3+}	0.260	0.226
Pr^{3+}	0.002	0.002	-	0.001	La^{3+}	0.002	0.000	Pr^{3+}	0.001	Sm^{3+}	0.205	0.197	0.236	0.241	0.242	0.029	0.076	Ho^{3+}	0.033	0.021
Nd^{3+}	0.002	0.000	-	0.000	Ce^{3+}	0.004	0.005	Nd^{3+}	0.000	Eu^{3+}	0.004	0.001	0.022	0.021	0.022	0.010	0.017	Er^{3+}	0.069	0.036
Sm^{3+}	0.005	0.003	-	0.006	Pr^{3+}	0.000	0.000	Sm^{3+}	0.003	Gd^{3+}	0.132	0.146	0.173	0.299	0.312	0.097	0.361	Tm^{3+}	0.009	0.030
Eu^{3+}	0.002	0.003	-	0.003	Nd^{3+}	0.005	0.017	Eu^{3+}	0.002	Tb^{3+}	0.009	0.010	0.008	0.020	0.021	0.018	0.047	Yb^{3+}	0.041	0.014
Gd^{3+}	0.009	0.007	-	0.000	Sm^{3+}	0.004	0.027	Gd^{3+}	0.002	Dy^{3+}	0.015	0.013	0.012	0.032	0.030	0.090	0.129	Lu^{3+}	0.025	0.016
Tb^{3+}	0.003	0.003	-	0.016	Eu^{3+}	0.000	0.004	Tb^{3+}	0.000	Ho^{3+}	0.001	0.006	0.001	0.003	0.003	0.009	0.005	Ca^{2+}	0.058	0.059
Dy^{3+}	0.005	0.011	-	0.009	Gd^{3+}	0.000	0.039	Dy^{3+}	0.003	Er^{3+}	0.003	0.001	0.002	0.003	0.001	0.037	0.008	Ba^{2+}	-	0.009
Ho^{3+}	0.001	0.001	-	0.000	Tb^{3+}	0.001	0.005	Ho^{3+}	0.001	Tm^{3+}	0.000	0.000	0.001	0.000	0.000	0.009	0.001	Total A	1.950	1.916
Er^{3+}	0.003	0.012	-	-	Dy^{3+}	0.001	0.030	Er^{3+}	0.001	Yb^{3+}	0.002	0.003	0.002	0.003	0.004	0.03	0.004	Fe^{2+}	0.445	0.130
Tm^{3+}	0.001	0.001	-	-	Ho^{3+}	0.000	0.003	Tm^{3+}	0.001	Lu^{3+}	0.001	0.000	0.000	0.000	0.000	0.004	0.001	Mn^{2+}	0.000	0.002
Yb^{3+}	0.000	0.007	-	-	Er^{3+}	0.001	0.006	Yb^{3+}	0.000	Ca^{2+}	0.014	0.012	0.007	0.021	0.004	0.003	0.000	Mg^{2+}	0.000	0.000
Lu^{3+}	0.001	0.000	-	-	Tm^{3+}	0.000	0.003	Lu^{3+}	0.000	Sr^{2+}	0.002	-	0.001	-	-	-	-	Al^{3+}	0.000	-
Ca^{2+}	0.020	0.002	0.012	0.000	Yb^{3+}	0.000	0.007	Ca^{2+}	4.977	Fe^{2+}	0.003	0.001	0.003	0.005	0.001	0.001	0.000	□	0.555	0.868
Sr^{2+}	0.000	0.000	0.008	0.000	Lu^{3+}	0.001	0.001	Sr^{2+}	0.000	Pb^{2+}	0.000	0.000	0.000	0.000	0.000	0.000	0.000	Total M	1.000	1.000
Fe^{2+}	0.008	0.000	0.016	0.000	Mn^{2+}	0.005	0.012	Ba^{2+}	0.000	Mn^{2+}	0.001	0.002	0.002	0.000	0.001	-	-	B^{3+}	0.188	0.229
Pb^{2+}	0.031	0.022	0.005	0.019	Mg^{2+}	0.005	0.000	Pb^{2+}	0.000	Total A	0.998	0.985	0.969	0.981	0.985	0.995	0.984	Be^{2+}	1.812	1.771
K^{+}	-	-	0.038	0.005	Ca^{2+}	0.102	0.138	Mn^{2+}	0.004	Total	2.003	1.996	1.989	1.998	1.994	1.995	1.993	Total Q	2.000	2.000
Total	0.945	1.002	0.609	1.016	Sr^{2+}	0.003	0.004	Fe^{2+}	0.001	X_{Ht}	1.66	0.06	0.73	0.70	0.12	-	-	Si^{4+}	1.983	1.909
					Pb^{2+}	0.014	0.003	Total M	5.000	X_{Cher}	0.00	1.18	0.00	1.43	0.37	-	-	P^{5+}	0.003	0.005
					K^{+}	0.011	0.008	OH^{-}_{calc}	0.000	X_{Mnz}	98.34	98.76	99.27	97.88	99.51	-	-	As^{5+}	0.015	0.086
					Total A	1.027	0.965	F^{-}	1.024									Total T	2.000	2.000
					Total	3.000	3.000	Cl^{-}	0.007									O^{2-}	0.890	0.264
								Total X	1.032									OH^{-}_{calc}	1.110	1.736
																		F^{-}	0.000	0.000
																		Total φ	2.000	2.000

Note: n.a. - not analyzed; int. = interior; recalc = recalculated. Urn = uraninite; Bnr = brannerite; Fap = fluorapatite; Mnz = monazite; Xtm = xenotime; Hin = hingganite.

Fig. 1

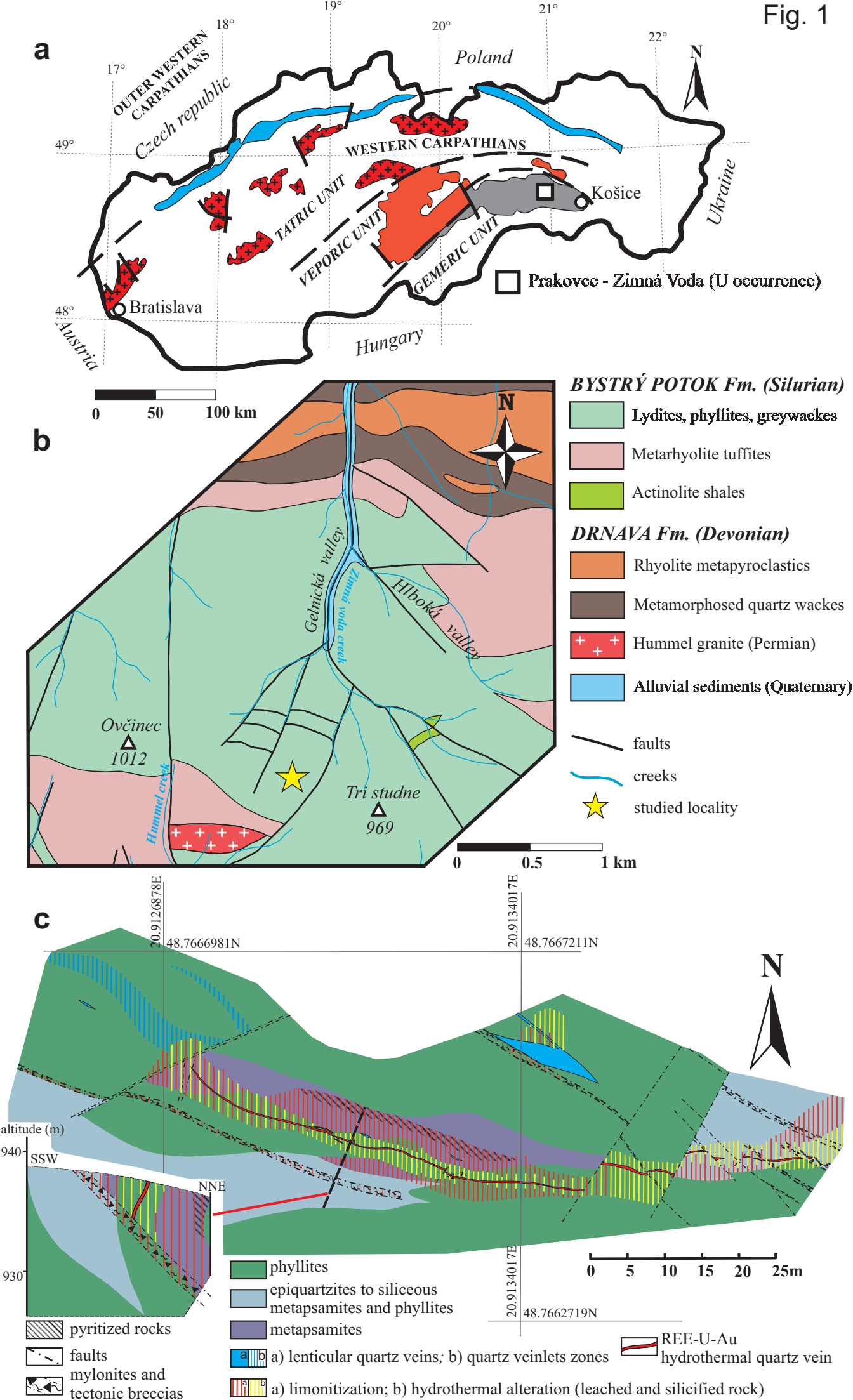
a
OUTER WESTERN CARPATHIANS
Czech republic
Poland
WESTERN CARPATHIANS
TATRIC UNIT
VEPORIC UNIT
GEMERIC UNIT
Košice
Ukraine
Bratislava
Austria
Hungary
Prakovce - Zimná Voda (U occurrence)
17°
18°
19°
20°
21°
22°
49°
48°
N
0 50 100 km
b
Gelnická valley
Zimná voda creek
Hlboká valley
Hummel creek
Ovčinec
1012
Tri studne
969
N
0 0.5 1 km
BYSTRÝ POTOK Fm. (Silurian)
Lydites, phyllites, greywackes
Metarhyolite tuffites
Actinolite shales
DRNAVA Fm. (Devonian)
Rhyolite metapyroclastics
Metamorphosed quartz wackes
Hummel granite (Permian)
Alluvial sediments (Quaternary)
faults
creeks
studied locality
c
20.9126878E
48.7666981N
20.9134017E
48.7667211N
N
altitude (m)
940
930
SSW
NNE
20.9134017E
48.7662719N
0 5 10 15 20 25m
phyllites
epiquartzites to siliceous metapsamites and phyllites
metapsamites
a) lenticular quartz veins; b) quartz veinlets zones
REE-U-Au hydrothermal quartz vein
a) limonitization; b) hydrothermal alteration (leached and silicified rock)
pyritized rocks
faults
mylonites and tectonic breccias

Fig. 2

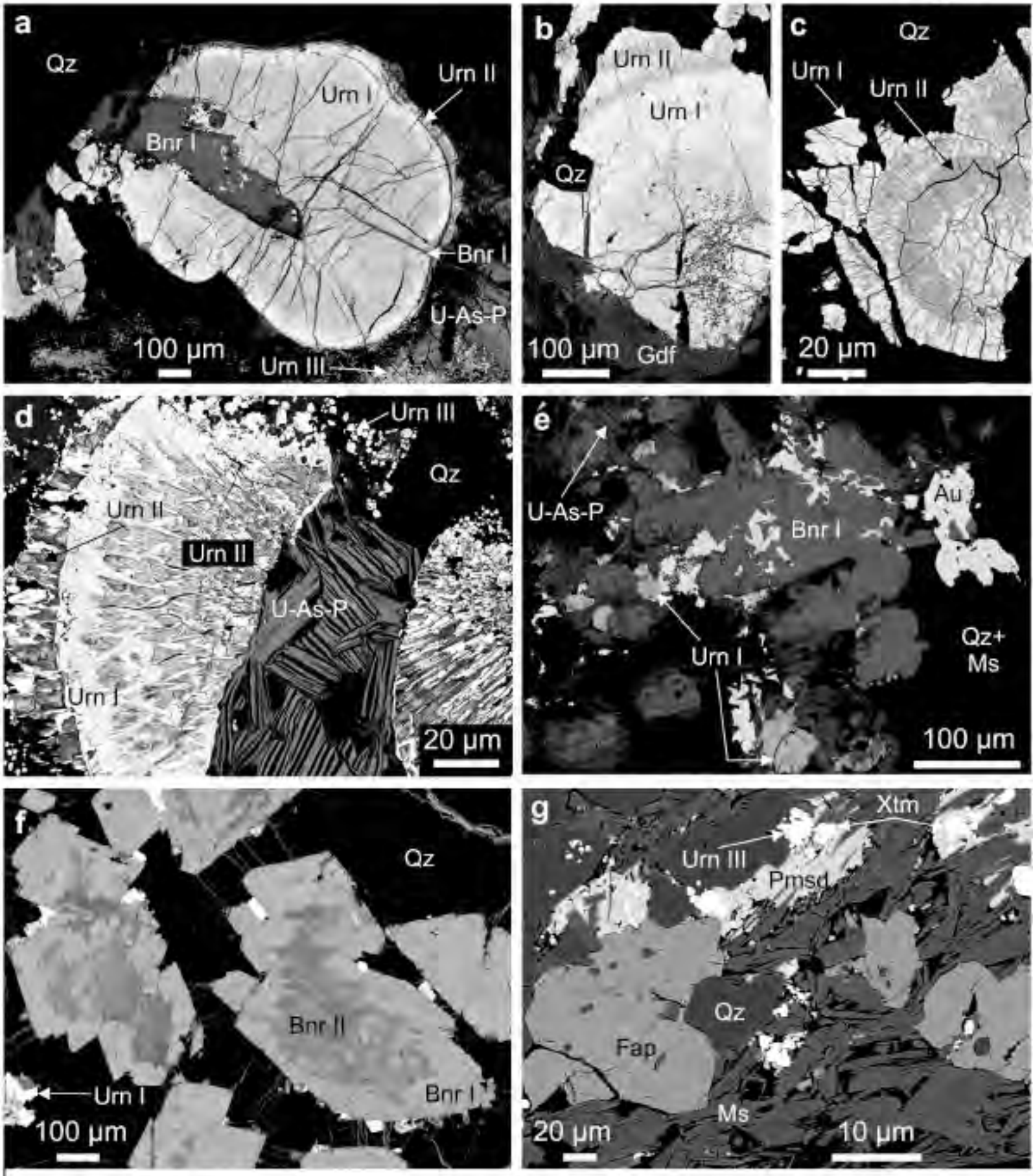
a
Qz
Urn II
Urn I
Bnr I
Bnr I
U-As-P
100 µm
Urn III
b
Urn II
Urn I
Qz
100 µm
Gdf
c
Qz
Urn I
Urn II
20 µm
d
Urn III
Qz
Urn II
Urn II
U-As-P
Urn I
20 µm
é
U-As-P
Au
Bnr I
Qz+
Ms
Urn I
100 µm
f
Qz
Bnr II
Urn I
Bnr I
100 µm
g
Xtm
Urn III
Pmsd
Qz
Fap
Ms
20 µm
10 µm

Fig. 3

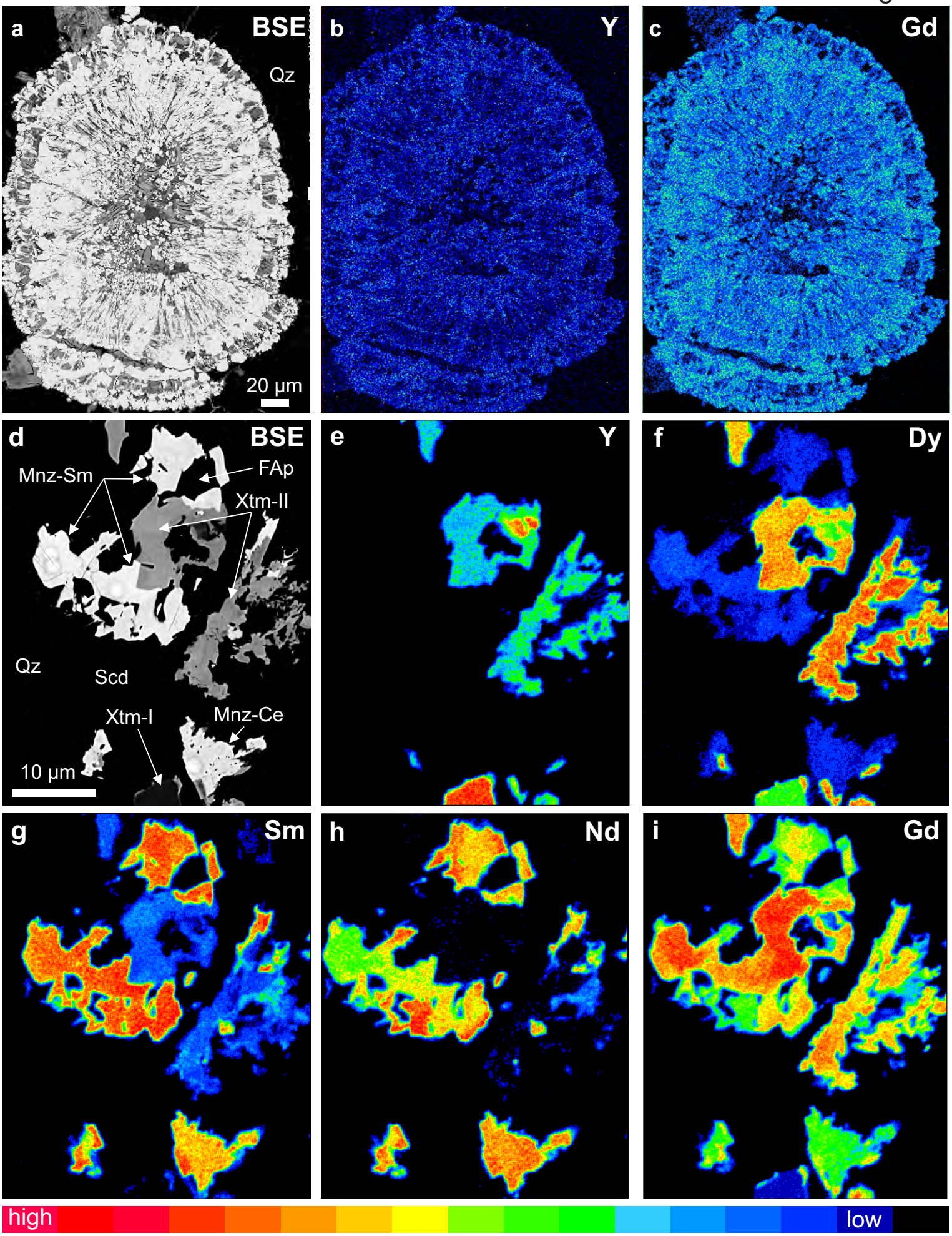
a
BSE
Qz
20 μm
b
Y
c
Gd
d
BSE
Mnz-Sm
FAp
Xtm-II
Qz
Scd
Xtm-I
Mnz-Ce
10 μm
e
Y
f
Dy
g
Sm
h
Nd
i
Gd
high
low

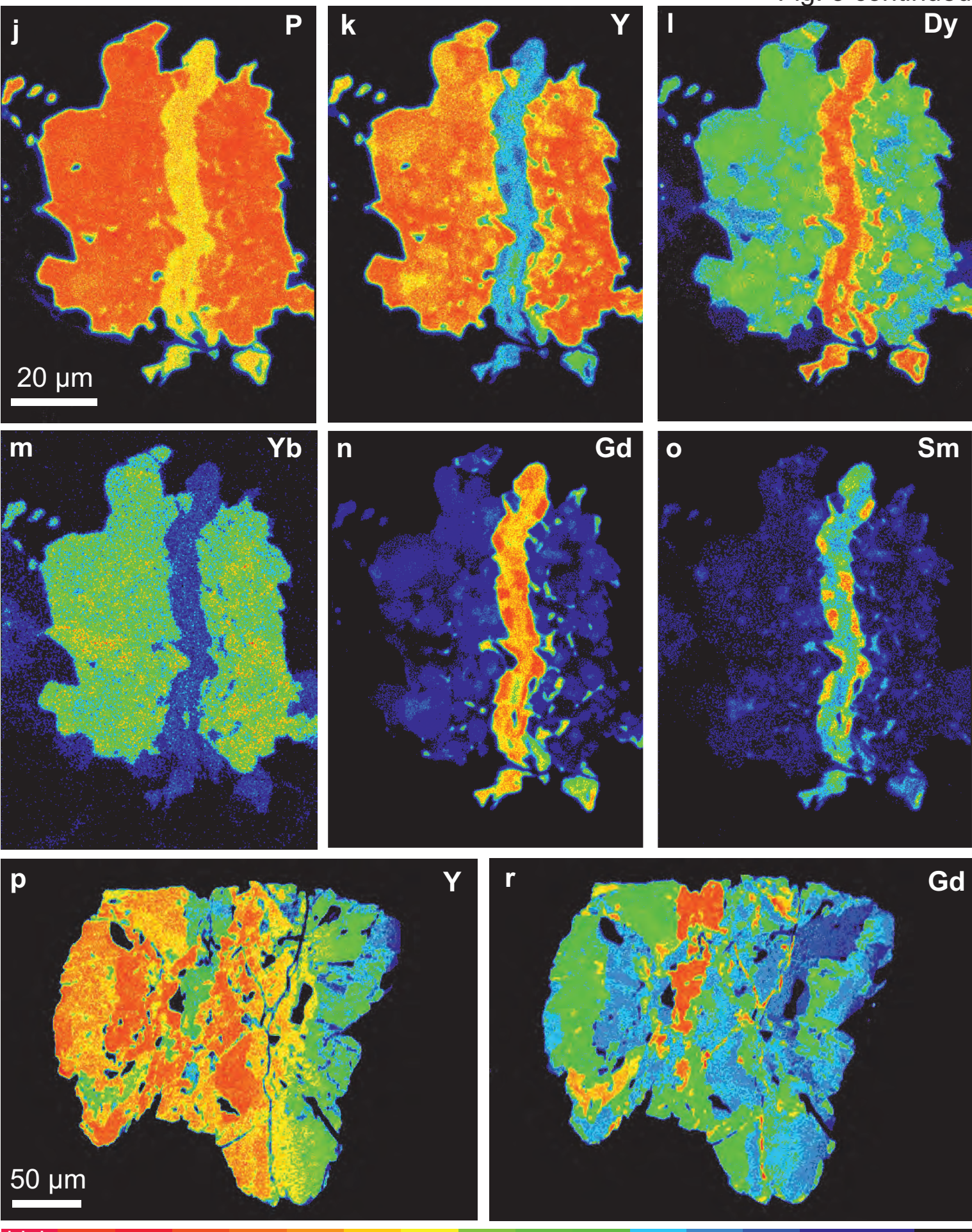
j
P
20 μm
k
Y
l
Dy
m
Yb
n
Gd
o
Sm
p
Y
50 μm
r
Gd
high
low

Fig. 4

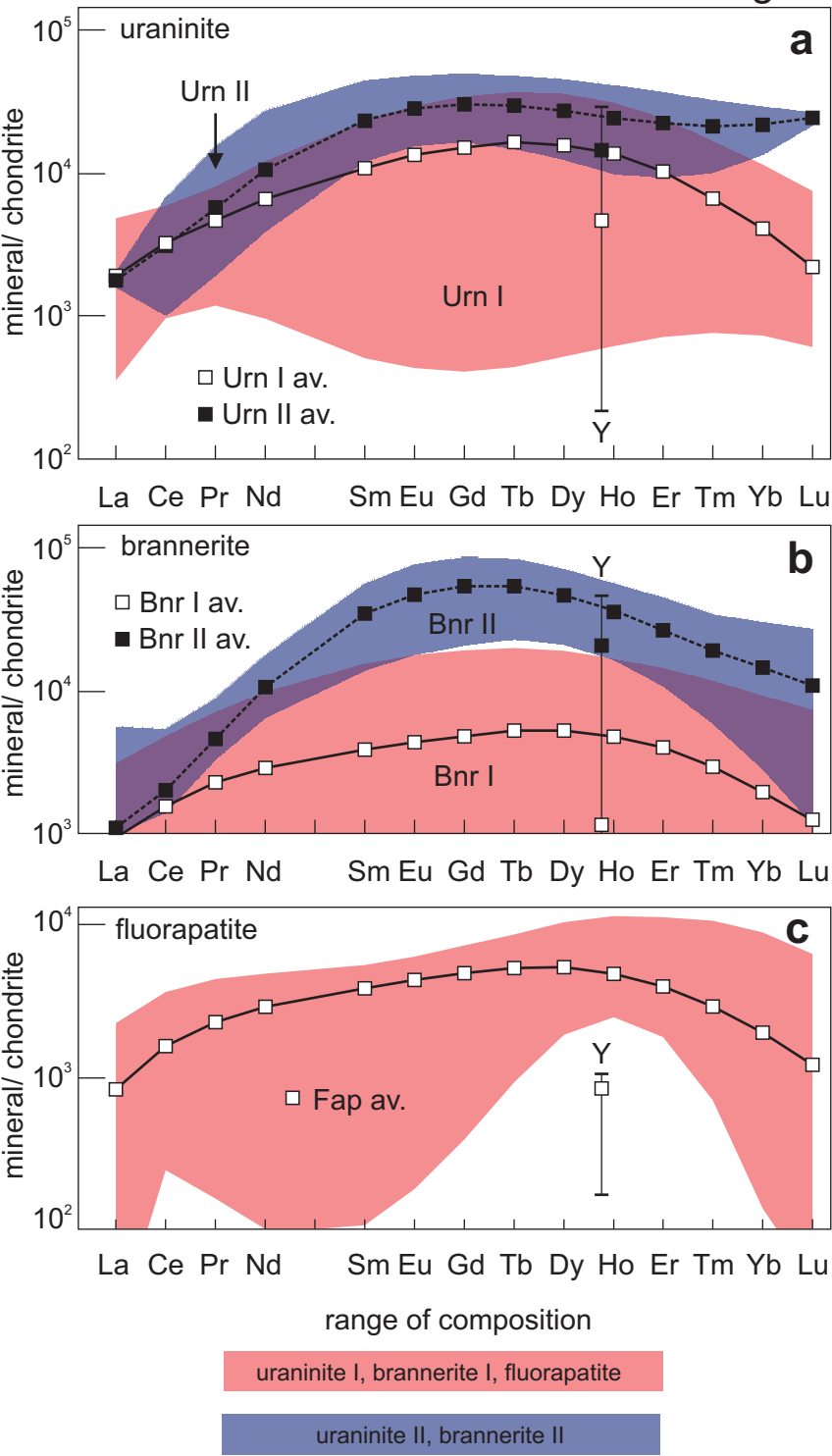
uraninite
a
Urn II
Urn I
Urn I av.
Urn II av.
Y
mineral/ chondrite
10^5
10^4
10^3
10^2
La Ce Pr Nd Sm Eu Gd Tb Dy Ho Er Tm Yb Lu
brannerite
b
Bnr I av.
Bnr II av.
Bnr II
Bnr I
Y
fluorapatite
c
Fap av.
range of composition
uraninite I, brannerite I, fluorapatite
uraninite II, brannerite II

Fig. 4 continued

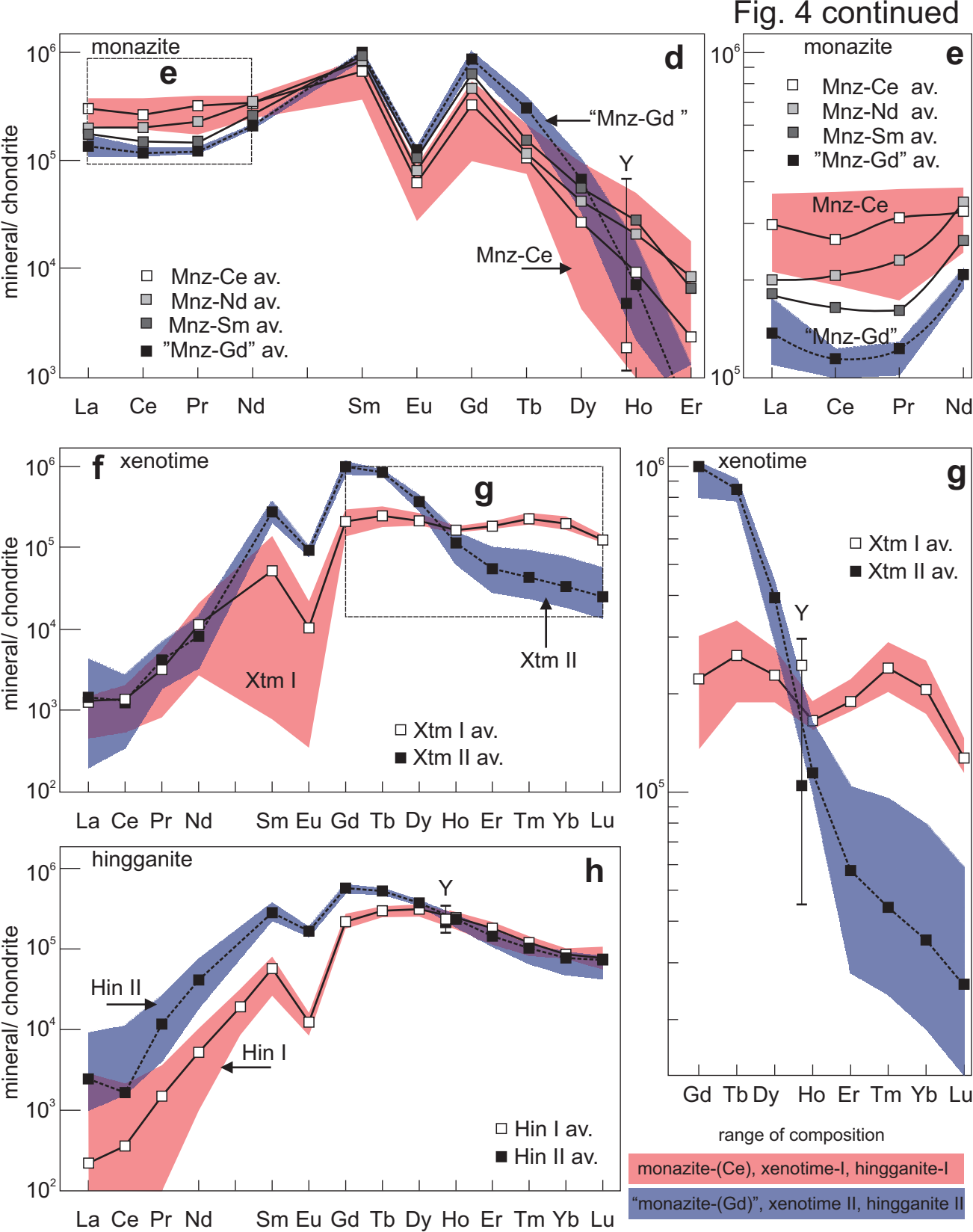

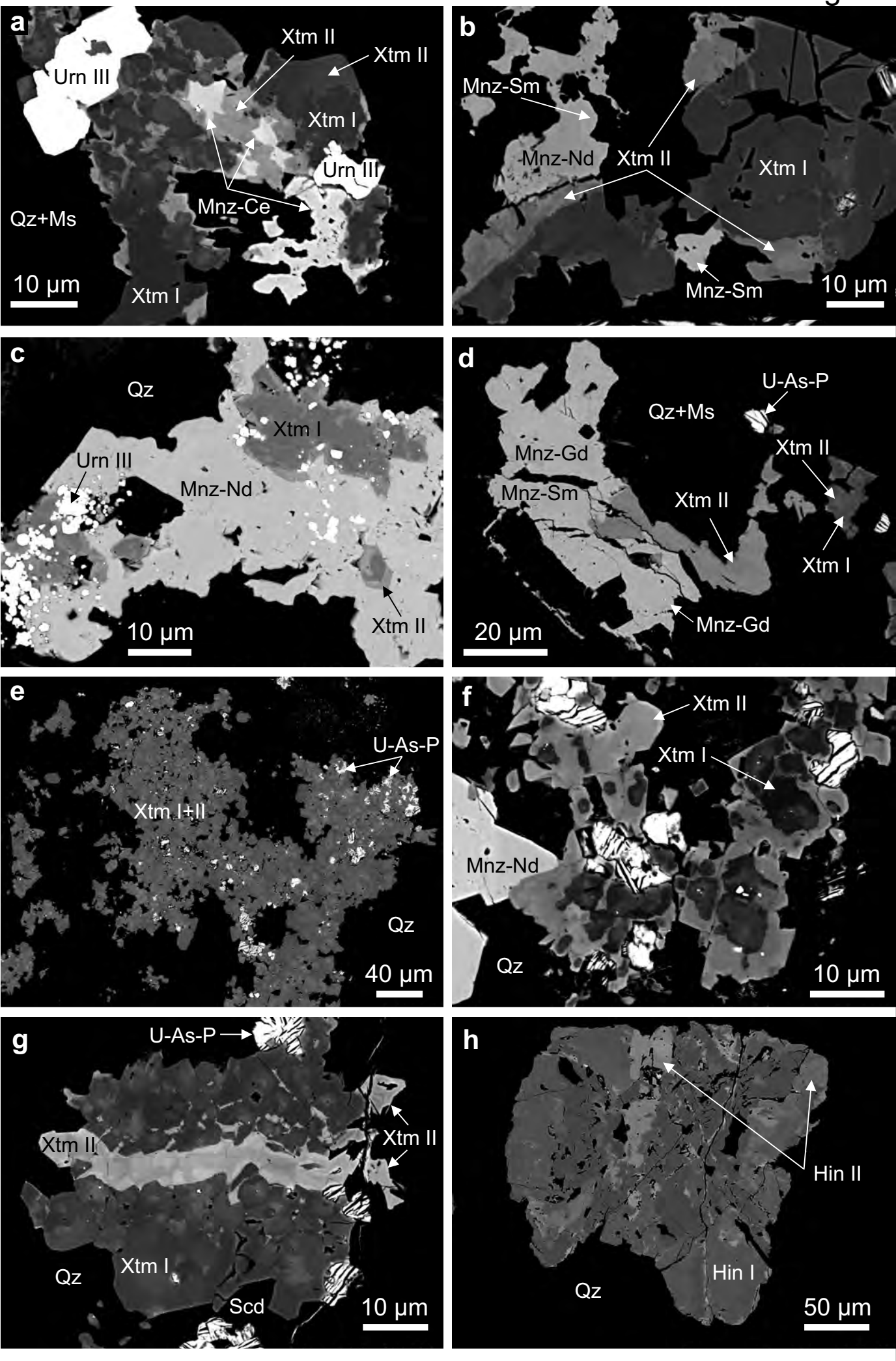
a
Xtm II
Xtm II
Urn III
Xtm I
Urn III
Mnz-Ce
Qz+Ms
10 μm
Xtm I
b
Mnz-Sm
Mnz-Nd
Xtm II
Xtm I
Mnz-Sm
10 μm
c
Qz
Xtm I
Urn III
Mnz-Nd
10 μm
Xtm II
d
U-As-P
Qz+Ms
Xtm II
Mnz-Gd
Mnz-Sm
Xtm II
Xtm I
20 μm
Mnz-Gd
e
U-As-P
Xtm I+II
Qz
40 μm
f
Xtm II
Xtm I
Mnz-Nd
Qz
10 μm
g
U-As-P
Xtm II
Xtm II
Qz
Xtm I
Scd
10 μm
h
Hin II
Hin I
Qz
50 μm

Fig. 6

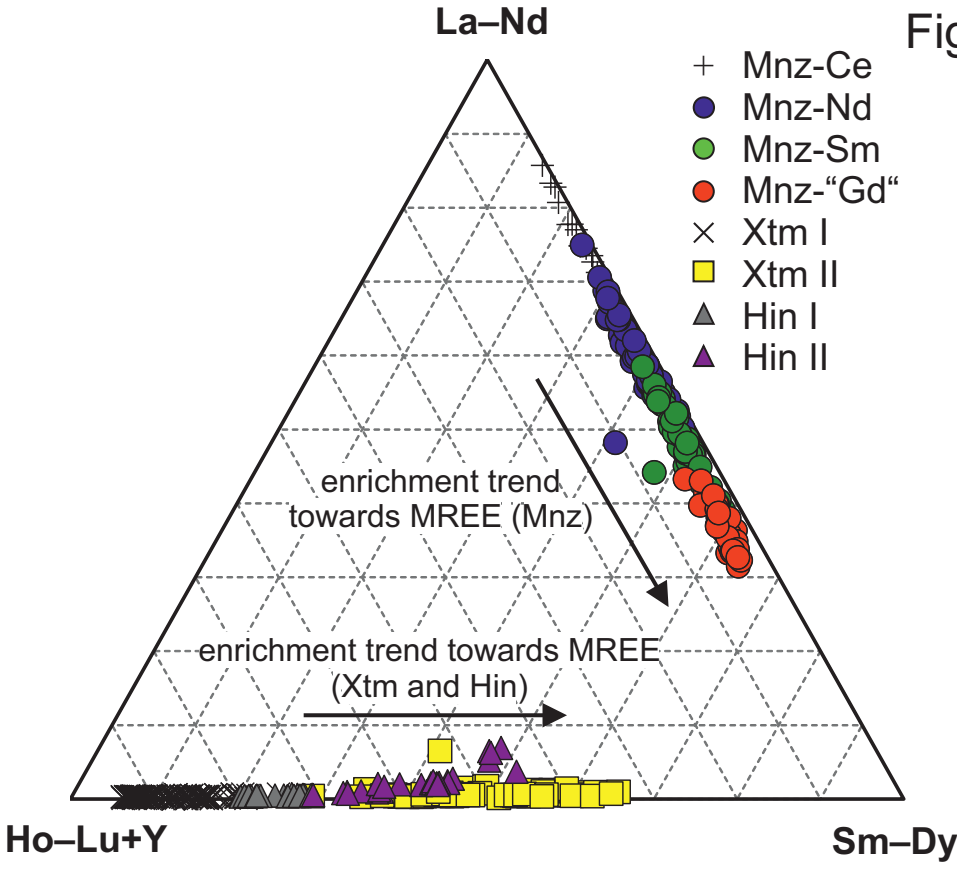
La–Nd
Mnz-Ce
Mnz-Nd
Mnz-Sm
Mnz-“Gd“
Xtm I
Xtm II
Hin I
Hin II
enrichment trend
towards MREE (Mnz)
enrichment trend towards MREE
(Xtm and Hin)
Ho–Lu+Y
Sm–Dy

Fig. 7

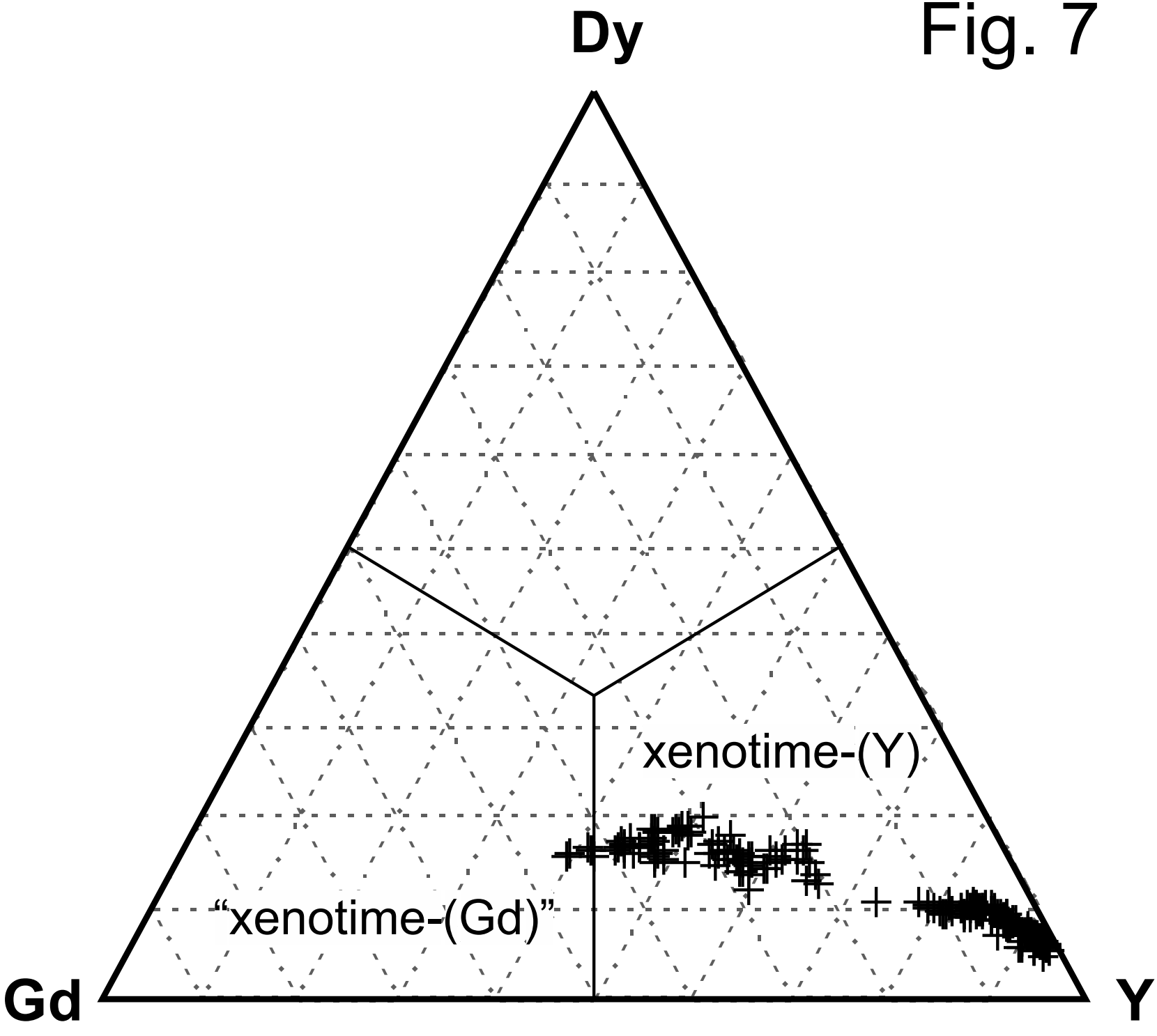

Fig. 8

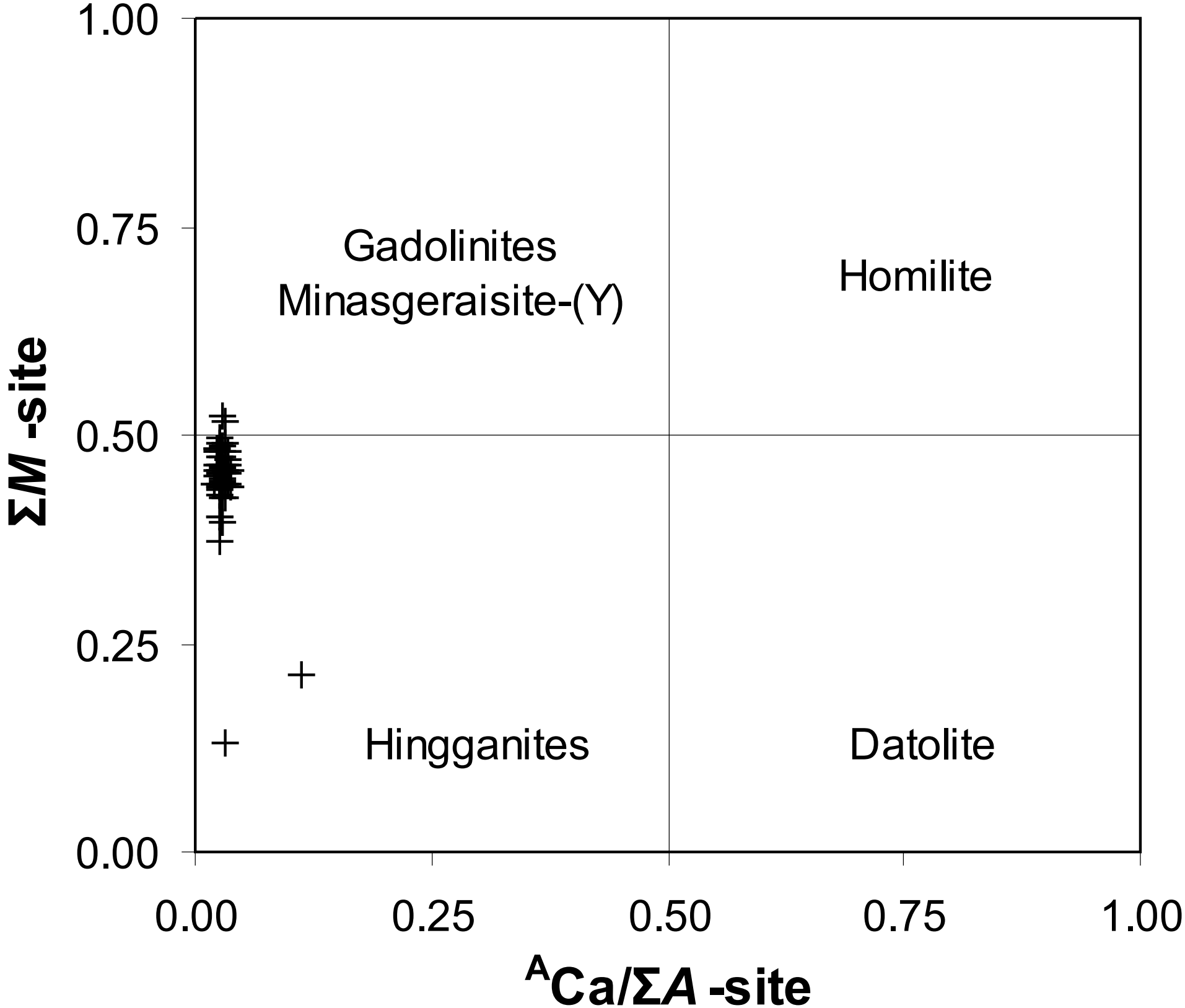
1.00
0.75
0.50
0.25
0.00
Gadolinites
Minasgeraisite-(Y)
Homilite
Hingganites
Datolite
ΣM -site
0.00
0.25
0.50
0.75
1.00
ACa/ΣA -site